

# Elliptic flow of inclusive electrons at $\sqrt{S_{NN}} = 2.76$ TeV Pb-Pb collisions with the ALICE detector

Lydia Brenner<sup>1</sup>

July 11, 2013

Supervisors: Raimond Snellings<sup>1,2</sup>, Andrea Dubla<sup>1</sup>

## Abstract

One of the main components in the study of the elliptic flow of heavy flavour decay electrons is the elliptic flow of inclusive electrons. There are several methods that can be applied to get the inclusive electron elliptic flow at  $\sqrt{S_{NN}} = 2.76$  TeV with the ALICE detector. However these methods are effected by contamination in the electron sample. This thesis demonstrates a method to remove contamination in the electron sample at the yield level and compares with the results of other methods. We find that the elliptic flow determined with this method is comparable within the error bars to all studied methods. This means that effect of the contamination of the electron sample on the elliptic flow is not visible in the other methods.

---

<sup>1</sup>Utrecht University

<sup>2</sup>NIKHEF

# Contents

<b>1</b>	<b>Motivation for the physics</b>	<b>1</b>
1.1	Quantum Chromodynamics . . . . .	2
<b>2</b>	<b>Introduction to flow</b>	<b>3</b>
2.1	Equation of state dependence . . . . .	6
2.2	The scalar product method . . . . .	11
2.3	The Q-cumulant method . . . . .	13
2.4	The event plane method . . . . .	15
2.4.1	$\phi - \Psi$ method for elliptic flow . . . . .	17
<b>3</b>	<b>Introduction to the detector</b>	<b>18</b>
3.1	The ALIROOT framework . . . . .	20
<b>4</b>	<b>Inclusive electron <math>v_2</math></b>	<b>21</b>
4.1	Event selection . . . . .	21
4.2	Track selection . . . . .	27
4.3	PID and cut optimisation . . . . .	28
4.4	Background estimation . . . . .	34
4.5	$\phi - \Psi$ method . . . . .	36
4.6	Results . . . . .	40
<b>5</b>	<b>systematics</b>	<b>41</b>
5.1	centrality estimator . . . . .	42
5.2	normalisation range . . . . .	43
5.3	binning . . . . .	44
5.4	Yield extraction . . . . .	45
5.4.1	Fitting routine . . . . .	45
5.4.2	Data driven method . . . . .	48
5.5	number of $\Delta\phi$ bins . . . . .	52
5.6	TPC $N\sigma$ range . . . . .	53
5.7	E/p range . . . . .	54
5.8	shower shape cut . . . . .	55
5.9	systematics summary . . . . .	56
<b>6</b>	<b>Conclusions, discussions and outlook</b>	<b>58</b>
	<b>Appendix</b>	<b>61</b>
	<b>References</b>	<b>81</b>

## List of Figures

1	reaction plane . . . . .	3
2	flow example . . . . .	5
3	sound velocity dependence on temperature . . . . .	6
4	Different EoS dence of $v_2$ . . . . .	8
5	The anisotropy in momentum space for two EoS . . . . .	9
6	The dependence on $\eta/s$ of $v_2$ for charged particles . . . . .	10
7	The alice detector . . . . .	18
8	vertex distribution . . . . .	22
9	centrality pass . . . . .	23
10	Multiplicity Fit . . . . .	24
11	Multiplicity Fit. Mean on the left, sigma on the right. . . . .	24
12	VZEROA event plane distribution . . . . .	26
13	VZEROC event plane distribution . . . . .	26
14	TPC n-sigma distribution before cut . . . . .	28
15	inclusive electron projection, E/p distribution . . . . .	29
16	shower shape cut . . . . .	30
17	M20 distribution before cut . . . . .	30
18	M02 distribution before cut . . . . .	31
19	M20 distribution in the selection range . . . . .	31
20	M02 distribution in the selection range . . . . .	32
21	Optimisation of the shower shape cut . . . . .	33
22	comparing background reduction, E/p $1.5 < p_T < 2$ , $\phi$ inte- grated . . . . .	35
23	purity comparison of electrons . . . . .	35
24	Raw Yield . . . . .	38
25	$v_2$ observed . . . . .	38
26	final $v_2$ . . . . .	39
27	method comparison for $v_2$ of inclusive electrons . . . . .	40
28	Cl1 and TRK comparison . . . . .	42
29	normalisation comparison . . . . .	43
30	binning comparison . . . . .	44
31	E/p distribution for $1.5 < p_T < 2$ . Colours as in equation (56) . . . . .	45
32	Raw Yield . . . . .	46
33	final $v_2$ . . . . .	47
34	E/p $1.5 < p_T < 2$ . . . . .	48
35	E/p $1.5 < p_T < 2$ . . . . .	49
36	Raw Yield . . . . .	50
37	method comparison . . . . .	51
38	number of delta phi bins comparison . . . . .	52

39	TPC $n\sigma$ comparison . . . . .	53
40	yield extraction comparison E/p range . . . . .	54
41	SS cuts comparison . . . . .	55
42	systematics for particle identification studies . . . . .	56
43	systematics of non particle identification studies . . . . .	57
44	combined systematics . . . . .	58
45	conclusion . . . . .	59

## List of Tables

1	Event selection cuts . . . . .	25
2	Track selection cuts for electron candidates . . . . .	27
3	Different shower shape cuts . . . . .	32
4	Electron identification cuts . . . . .	32
5	centrality estimator . . . . .	42
6	normalisation range . . . . .	43
7	binning . . . . .	44
8	yield extraction methods comparison . . . . .	51
9	number of delta phi bins . . . . .	52
10	TPC $n\sigma$ . . . . .	53
11	E/p range . . . . .	54
12	SS cuts . . . . .	55
13	systematics for particle identification studies . . . . .	56
14	systematics of non particle identification studies . . . . .	57
15	combined systematics . . . . .	58
16	absolute error . . . . .	58

# 1 Motivation for the physics

The ALICE (A Large Ion Collision Experiment) detector is mainly suited for studying the Quark-Gluon Plasma (QGP) and its properties. The QGP (Quark-Gluon Plasma) is the new phase of matter predicted by Quantum Chromodynamics formed at high energy density. Shortly after the big bang the universe is expected to have behaved as a QGP which hadronized as space itself expanded. In the Quark-Gluon Plasma particles experience extreme densities and temperatures. One of the fundamental questions in particle physics is therefore what the properties of matter at extreme densities and temperatures are. The QGP can not be studied directly, however the properties of it determine the evolution of the collision system. We call the collective expansion of the particles after the collision the flow of the system. For a non-central collision of two nuclei, the initial anisotropy in coordinate space is translated to a final anisotropy in momentum space. This effect can be characterised by the elliptic flow,  $v_2$ .

The anisotropic flow is the azimuthal anisotropy in the momentum-space distribution of the particles which is generated in non-central heavy-ion collisions as a result of initial asymmetry in the geometric. This anisotropic flow is quantified by Fourier coefficients of the azimuthal momentum distribution of outgoing particles in the transverse plane with respect to the reaction plane. Elliptic flow is one of the most sensitive probes of particle dynamics at the Large Hadron Collider (LHC).

In particular heavy flavour particles carry information about the full collision history since they are created in the first stages of the collision. Furthermore, due to their large mass, the gluon radiation is suppressed at small angles. This is called the dead cone effect.

By looking at heavy flavour decay electrons (HFe) there are some other benefits. Heavy flavour decay electrons have:

- A large branching ratio:  $O(10\%)$ .
- A large signal-to-background ratio at high  $p_T$ .
- The possibility to trigger on the electrons.

In particular in Pb-Pb collision we also get that:

- Heavy flavour electrons probe the level of thermalization of heavy quarks in the deconfined medium at low  $p_T$ .
- Heavy flavour electrons carry information about the energy loss of heavy quarks at high  $p_T$ .

There are several methods that can be applied to get the heavy flavour electron elliptic flow. Most of these methods however could be effected by contamination in the electron sample. This thesis reports a study to a method applied to remove the contamination at the electron yield level. Instead of studying heavy flavour electron flow this thesis only covers inclusive electron flow. Inclusive electron flow is the main components for heavy flavour electron flow.

## 1.1 Quantum Chromodynamics

The strong force in the Standard Model of particle physics is described by Quantum-Chromo-Dynamics (QCD). QCD is a non-abelian quantum field gauge theory, based on local colour symmetry of the  $SU(3)_C$  group.

The QCD lagrangian:

$$\mathcal{L}_{QCD} = \bar{q}(i\gamma^\mu\delta_\mu - m)q - g(\bar{q}\gamma^\mu T_a q)G_\mu^a - \frac{1}{4}G_{\mu\nu}^a G_a^{\mu\nu} \quad (1)$$

where  $q$  denote quark fields,  $G_\mu^a$  are the gluon fields,  $\gamma^\mu$  are the Dirac matrices,  $T_a$  denote  $SU(3)$  group generators and  $m$  is the mass. QCD describes interacting quarks that carrying colour and interact with a massless vector gluon field to which the quarks couple with strength  $g$ .

In formula (1)  $G_{\mu\nu}^a$  is given by

$$G_{\mu\nu}^a = \delta_\mu G_\nu^a - \delta_\nu G_\mu^a - gf_{abc}G_\mu^b G_\nu^c \quad (2)$$

The third term in this equation induces a self-interaction between the gauge bosons. This can be seen more clearly if we rewrite the lagrangian in symbolic form:

$$\mathcal{L}_{QCD} = \bar{q}q + G^2 + g\bar{q}qG + gG^3 + g^2G^4 \quad (3)$$

The first three terms in this lagrangian describe the free propagation of quarks and gluons and the quark-gluon interactions. The last two terms show the presence of three and four gluon vertices in QCD and reflect gluons themselves carry colour charge.

Since there is only one coupling  $g$  gauge invariance uniquely determines the structure of the gluon self-coupling terms.

The three and four point interactions give rise to the running coupling constant  $\alpha_s$ . One of the important consequences for particle dynamics on QCD is *confinement*. At low energies the coupling constant  $\alpha_s$  is very large. Because of the high coupling constant quarks and gluons are confined to bound states and form hadrons.

## 2 Introduction to flow

Heavy-ions created in a head-on collision differ from those created in a peripheral collisions. We categorise the collisions by their centrality, which is defined by the impact parameter  $b$ .  $b$  is the distance between the two centres of the colliding ions.

Flow signals the presence of multiple interactions between the constituents of the medium created in the collision. More interactions usually leads to a larger magnitude of the flow and brings the system closer to thermalization. The magnitude of the anisotropic flow is therefore a detailed probe of the level of thermalization.

Experimentally, the most direct evidence of flow comes from the observation of the anisotropy in particle momentum distributions correlated with the reaction plane. The reaction plane is defined by the impact parameter and the beam direction  $z$ . A convenient way of characterising the various patterns of anisotropic flow is to use a Fourier expansion of the invariant triple differential distributions:

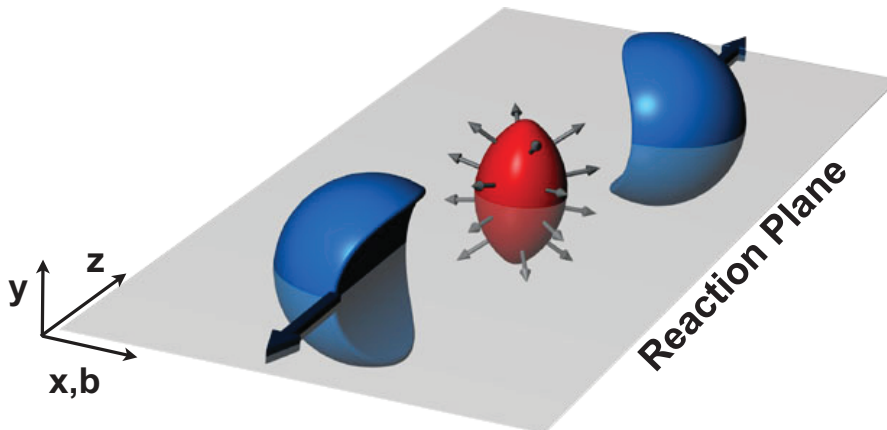


Figure 1: reaction plane. Reproduced from [13].

$$E \frac{d^3 N}{d^3 p} = \frac{d^3 N}{p_T dp_T dy d[\phi - \Psi_n]} = \frac{1}{2\pi} \frac{d^2 N}{p_t dp_t dy} \left( 1 + \sum_{n=1}^{\infty} 2v_n(p_t, y) \cos[n(\phi - \Psi_n)] \right) \quad (4)$$

where  $E$  is the energy of the particle,  $p$  the momentum,  $p_T$  the transverse momentum,  $\phi$  the azimuthal angle,  $y$  the rapidity, and  $\Psi_n$  the reaction plane

angle.

The Fourier coefficients are  $p_T$  and  $y$  dependent and are given by

$$v_n(p_T, y) = \langle \cos[n(\phi - \Psi_n)] \rangle \quad (5)$$

where the angular brackets denote an average over the particles, summed over all events, in the  $(p_T, y)$  bin under study. In this Fourier decomposition, the coefficients  $v_1$  and  $v_2$  are known as directed and elliptic flow, respectively. Equation (4) is the average over the particles, summed over all events in the  $(p_T, y)$  bin that you are studying. The  $v_n$  in this Fourier series are the flow components.  $v_1$  is called the directed flow and  $v_2$  is called the elliptic flow. The integrated flow is defined as an average, evaluated with  $\frac{d^2N}{dp_T dy}$  used as a weight. [1]

If we now look at  $\langle \frac{dN}{d\varphi} \rangle$  we see that for  $v_1$  the sum of momenta of particles has a preferred direction at a given rapidity. For  $v_2$  we see that the particle distribution shows an elliptic deformation.

The physical effects of the elliptic flow are that the reaction zone is anisotropic in the transverse plane. The anisotropy of the reaction zone is characterised by spatial eccentricity:

$$\epsilon = \frac{\langle y^2 - x^2 \rangle}{\langle y^2 + x^2 \rangle} \quad (6)$$

where  $x$  and  $y$  are the positions of the participating nucleons in the transverse plane and the average is taken over the number of participants.

Because the reaction plane angle is not a direct observable the elliptic flow can not be measured directly so that it is usually estimated using azimuthal correlations between the observed particles. Two-particle azimuthal correlations, for example, can be written as:

$$\begin{aligned} \langle \langle e^{2i(\phi_1 - \phi_2)} \rangle \rangle &= \langle \langle e^{2i(\phi_1 - \Psi_2 - (\phi_2 - \Psi_2))} \rangle \rangle \\ &= \langle \langle e^{2i(\phi_1 - \Psi_2)} \rangle \langle e^{-2i(\phi_2 - \Psi_2)} \rangle + \delta_2 \rangle \\ &= \langle v_2^2 + \delta_2 \rangle \end{aligned} \quad (7)$$

where the double brackets denote an average over all particles within an event, followed by averaging over all events. In Eq. 5 we have factorized the azimuthal correlation between the particles in a common correlation with the reaction plane (elliptic flow  $v_2$ ) and a correlation independent of the reaction plane (non-flow  $\delta_2$ ). Here we have assumed that the correlation between  $v_2$



and  $\delta_2$  is negligible. If  $\delta_2$  is small, Eq. 5 can be used to measure  $\langle v_2 \rangle$ , but in general the non-flow contribution is not negligible.

We illustrate two-particle nonflow contributions as follows: In Fig. 2a an anisotropic distribution is shown for which both  $v_2 = \langle \cos 2\phi \rangle$  and the two-particle correlation  $v_2\{2\} = \sqrt{\langle \cos 2(\phi_1 - \phi_2) \rangle}$  are positive. Figure 2b shows a symmetric distribution for which  $v_2 = 0$  and also  $v_2\{2\} = 0$ . Figure 2c shows two symmetric distributions rotated with respect to each other which give  $v_2 = 0$  while  $v_2\{2\}$  is nonzero. This illustrates how non-flow contributions from sources like resonance decays or jets can contribute to  $v_2$  measured from two particle correlations.

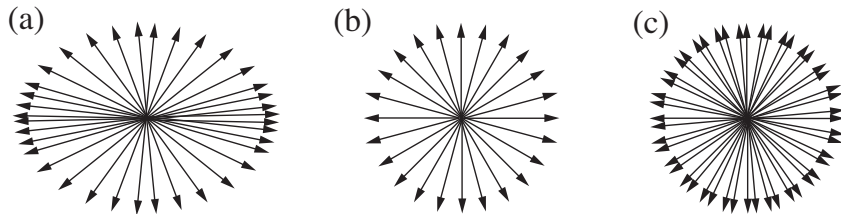


Figure 2: flow example (a) flow and 2-particle correlation  $> 0$  (b) flow and 2-particle correlation 0 flow 0 and 2-particle correlation  $> 0$ . Reproduced from [13].

## 2.1 Equation of state dependence

Elliptic flow depends on fundamental properties of the created matter such as sound velocity, shear viscosity and initial spatial eccentricity. This dependence can be calculated from measurements of elliptic flow as a function of transverse momentum, particle mass and collision centrality. However the magnitude and  $p_t$ -dependence of  $v_2$  depend on the equation of state (EoS). This means that elliptic flow also gives information on the equation of state, for example whether the EoS is closer to a lattice inspired EoS or closer to an EoS which incorporates a first order phase transition.

Let us first go back a bit to see where this EoS dependence comes from. As you can see in figure 3 the temperature (T) dependence of the velocity of sound ( $c_s = \sqrt{\partial P / \partial \epsilon}$ ) differs significantly between the different equations of state.

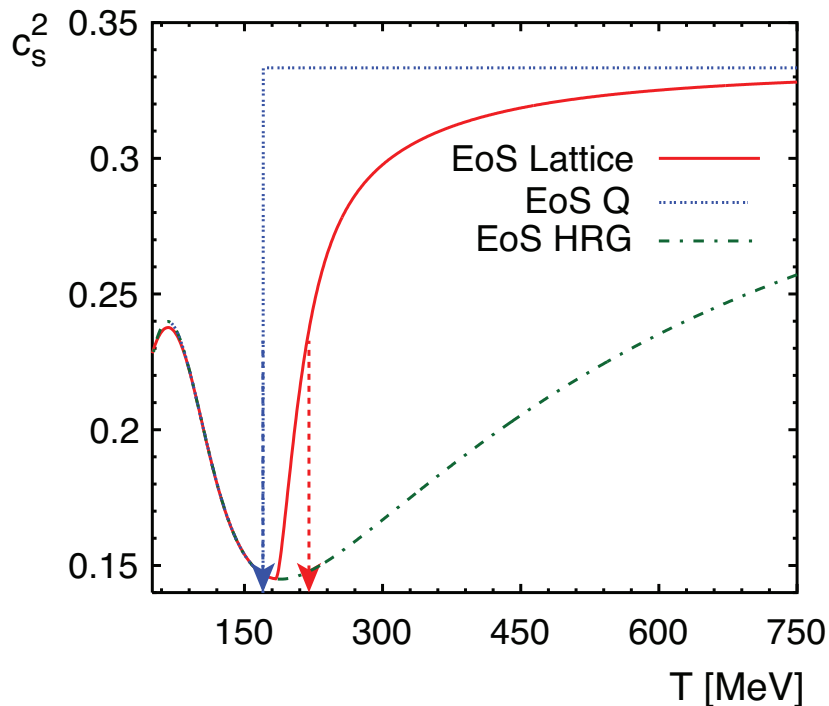


Figure 3: The dependence of the velocity of sound squared on temperature, for three different equations of state. Reproduced from [8].

*EoS Lattice* is a parametrization of the equation of state that matches recent lattice calculations. *EoS Q* is an equation of state that incorporates a first order phase transition. *EoS HRG* stands for the hadron resonance gas equation of state. The arrows indicate the corresponding transition temperatures for *EoS lattice* and *EoS Q*.

Model calculations show that this will have a clear signature in the flow.[8]

For large momenta we expect that the quarks and gluons interact weakly and that the QGP will behave as an ideal gas. For a mass-less gas the EoS is given by (This is also called the Stefan-Boltzmann limit):

$$P = \frac{1}{3}\epsilon \quad (8)$$

and

$$\epsilon = g \frac{\pi^2}{30} T^4 \quad (9)$$

Where  $P$  is the pressure,  $\epsilon$  the energy density,  $T$  the temperature and  $g$  the effective number of degrees of freedom. The effective number of degrees of freedom can be calculated using:

$$g = g_b + \frac{7}{8}g_f \quad (10)$$

Where  $g_b$  is the bosonic degrees of freedom and  $g_f$  the fermionic. For a three flavour QGP we have  $g = 47.5$  which is an order of magnitude larger than that of a pion gas where  $g \sim 3$ . For large temperatures the energy density comes quite close ( $\sim 0.9$ ) to the Stefan-Boltzmann limit.

We see that for low transverse momentum both equations of state show a mass dependence of  $v_2$ . We also see that the difference between *EoS Lattice* and *EoS Q* does not change much for the pion  $v_2$  while the  $v_2$  of protons does change significantly. This can be explained by the fact that heavier particles are more sensitive to the change in collective motion. This also means that the measured  $v_2$  for different particle species gives a constraint on the EoS in ideal hydrodynamics.

Another effect that differs for different equations of state is the build up of the flow. The initial almond shaped anisotropy in coordinate space vanishes, while the momentum space distribution changes in the opposite direction. The momentum space distribution will start by being approximately

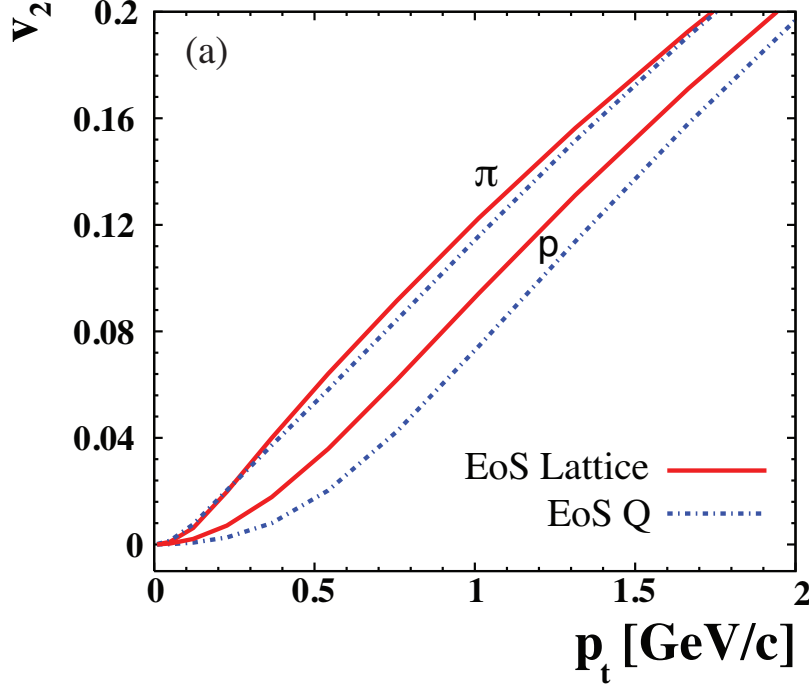


Figure 4: The different EoS dependence of  $v_2$  for pions and protons. Reproduced from [13].

azimuthally symmetric and changes to have a preferred direction in the reaction plane. The asymmetry in momentum space can be quantified by:

$$\epsilon_p = \frac{\langle T_{xx} - T_{yy} \rangle}{\langle T_{xx} + T_{yy} \rangle} \quad (11)$$

where  $T_{xx}$  and  $T_{yy}$  are the diagonal transverse components of the energy momentum tensor and the average is taken over the transverse plane. The general form of the energy momentum tensor in the  $\mu$ -direction per unit 3-surface perpendicular to the  $r$ -direction is:

$$T^{\mu\nu} = (\epsilon + P)u^\mu u^\nu - P g^{\mu\nu} \quad (12)$$

The asymmetry in momentum space is shown in figure 5. [13]

Note that to determine the energy momentum tensor you need the EoS, but also conservation rules, such as conservation of energy-momentum ( $\partial_\mu T^{\mu\nu} = 0$ ), conservation of baryon number ( $\partial_\mu(\rho_B u^\mu)$ ) and conservation of entropy current ( $\partial_\mu(su^\mu)$ ). The conservation of energy-momentum can also be written as  $u^\mu \partial_\mu \epsilon + (\epsilon + P)\partial_\mu u^\mu = 0$ .

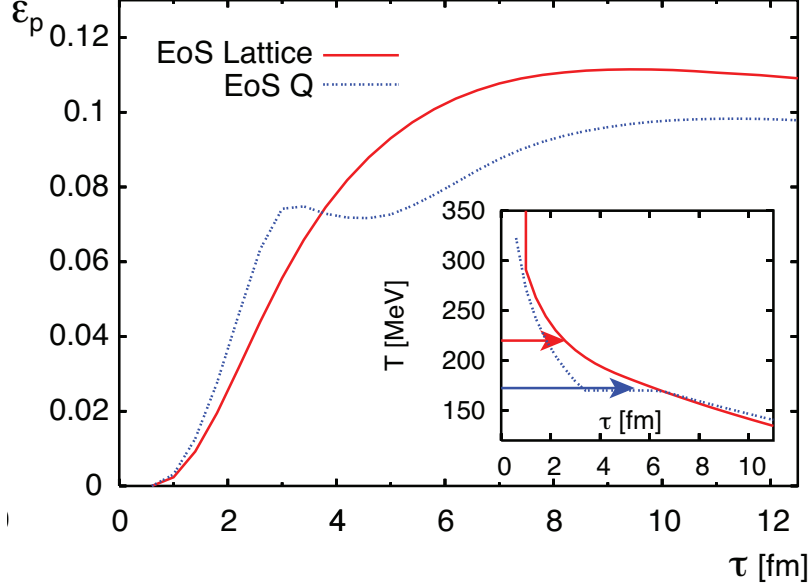


Figure 5: The anisotropy in momentum space for two EoS. Reproduced from [13].

Something else that influences on the build up of the elliptic flow are small deviations from ideal hydrodynamics, in particular viscous corrections. For relativistic fluids a useful quantity is the shear viscosity over entropy ratio  $\eta/s$ , where a small viscosity  $\eta$  means that it is a good fluid that does not convert much kinetic energy of the flow into heat. Known good fluids have an  $\eta/s$  of the order  $\frac{\hbar}{4\pi k_B}$ . Theory suggests that the transition from hadrons to quarks and gluons (as in a heavy-ion collision) occurs near the minimum in  $\eta/s$ , just as the phase transitions in helium, nitrogen and water. Careful measurements of  $\eta/s$  would therefore give precise information on the location of the transition. The effect of different  $\eta/s$  is shown in figure 6.[13]

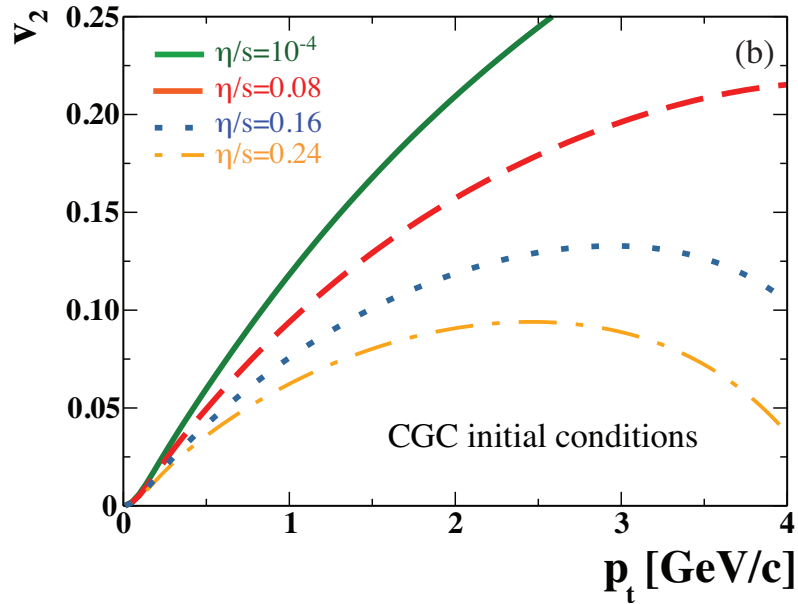


Figure 6: The dependence on  $\eta/s$  of  $v_2$  for charged particles. Reproduced from [13].

## 2.2 The scalar product method

In this analysis the elliptic flow determined with the SP method is done using the flow package. The method is shortly explained below.

The scalar product (SP) method as well as the Q-cumulant method which will be described later directly estimates  $v_n$  from multi-particle correlation and therefore does not depend on explicit construction of an (sub)event plane. The two-particle correlation of particles of interest is statistically unfavourable so we start by labelling all particles in an event as either reference particles (RP) or particles of interest (POI). In this study electrons will be used as particles of interest and all charged particles which pass the selection cuts will be used as reference particles. The RP and POI selections are divided into sub-events which are taken from different  $\eta$  ranges.

This gives the following for the flow of the particles of interest<sup>3</sup>

$$\begin{aligned} v_n^{POI} &= \sqrt{\langle e^{ni(\phi_i^{POI} - \phi_j^{POI})} \rangle} \\ &= \frac{\langle e^{ni(\phi_i^{POI} - \phi_j^{RP})} \rangle}{\langle e^{ni(\phi_i^{RP} - \phi_j^{RP})} \rangle} = \frac{v_n^{POI} \cdot v_n^{RP}}{\sqrt{v_n^{RP} \cdot v_n^{RP}}} \end{aligned} \quad (13)$$

We now define the following

$$u_k = e^{in\phi_k} \quad (14)$$

which is correlated with the complex-conjugate of the Q-vector from reference particles. In general the Q-vector is defined as

$$Q_n = \sum_{i=1}^M e^{in\phi_i} \quad (15)$$

where M is the multiplicity of the event and  $\phi_i$  is the azimuthal angle of an outgoing track in the laboratory frame.

If we now take the scalar product of  $u_k$  with  $Q_a^*$  where  $a$  denotes a given sub-event  $a$ , we get

$$u_k \cdot Q_a^* = e^{in\phi_k} \cdot \sum_{j=1, j \neq k}^{M_{RP,a}} e^{-in\phi_j} \quad (16)$$

where  $M_{RP,a}$  denotes reference particle multiplicity for a given sub-event  $a$  and  $j \neq k$  removes auto-correlations.

<sup>3</sup>note that since the RP and POI are selected within one event, the event plane is the same for all particles.

From this we get

$$\langle u \cdot Q_a^* \rangle = \frac{1}{M_{POI}} \sum_{i=k}^{M_{RP,a}} (e^{in\phi_k} \sum_{j=1, j \neq k}^{M_{RP,a}} e^{-in\phi_j}) \quad (17)$$

If we now use that  $M_{POI} = M_{RP,a} - k$  and that for any function  $f(x)$  and constant  $a$  we have

$$\sum a f(x) = a \sum f(x) \quad (18)$$

we get

$$\langle u \cdot Q_a^* \rangle = \frac{1}{M_{RP,a} - k} \sum_{i=k}^{M_{RP,a}} e^{in[\phi_k - \Psi_n]} \sum_{j=1}^{M_{RP,a}} e^{in[\phi_j - \Psi_n]} \quad (19)$$

If we now use

$$v_n = \frac{\sum_i^M e^{in[\phi - \Psi_n]}}{M} \quad (20)$$

we get

$$\langle u \cdot Q_a^* \rangle = M_{RP,a} v_n^{POI} v_n^{RP,a} \quad (21)$$

Continuing in the same way we get that for two sub-events  $a$  and  $b$  we get

$$v_2\{SP\} = \frac{1}{2} \left( \frac{\langle u_i \cdot Q_a/M_a \rangle}{\sqrt{\langle Q_a/M_a \cdot Q_b/M_b \rangle}} + \frac{\langle u_j \cdot Q_b/M_b \rangle}{\sqrt{\langle Q_a/M_a \cdot Q_b/M_b \rangle}} \right) \quad (22)$$



### 2.3 The Q-cumulant method

In this analysis the elliptic flow determined with the Q-cumulant (QC) method is done using the flow package. The method is shortly explained below.

The QC method has its strength in suppressing non-flow contributions by using cumulants. Cumulants are genuine multi-particle correlations. For example the two particle cumulant  $c_2\{2\}$  is defined as follows

$$c_2\{2\}^2 = \langle\langle e^{2i(\phi_1 - \phi_2)} \rangle\rangle = \langle v_2^2 + \delta_2 \rangle \quad (23)$$

We can improve the method introduced above by adding multi-particle correlations. For example we can add a 4-particle correlation:

$$c_2\{4\} = \langle\langle e^{2i(\psi_1 + \psi_2 - \psi_3 - \psi_4)} \rangle\rangle - 2\langle\langle e^{2i(\psi_1 - \psi_2)} \rangle\rangle^2 \quad (24)$$

which can be simplified to

$$c_2\{4\} = \langle v_2^4 + \delta_4 + 4v_2^2\delta_2 + 2\delta_2^2 \rangle - 2\langle v_2^2 + \delta_2 \rangle^2 = \langle -v_2^4 + \delta_4 \rangle \quad (25)$$

It can be shown that  $\delta_2 \propto 1/M_c$  and  $\delta_4 \propto 1/M_c^3$ , where  $M_c$  is the number of independent particle clusters.

This means that  $v_2\{2\} = \sqrt{\langle \cos 2(\phi_1 - \phi_2) \rangle}$  is only a good estimator if  $v_2 \gg 1/\sqrt{M_c}$  and  $v_2\{4\}$ , which is the flow estimate from  $c_2\{4\}$ , is a good estimator if  $v_2 \gg 1/M_c^{\frac{3}{4}}$ . The most direct approach would be to add an infinite number of correlations, which would eventually lead to  $v_2 \gg 1/M_c$ . Multi-particle correlations are often calculated from generating functions with numerical interpolations or from an exact solution.

We assumed that  $v_2$  and  $\delta_2$  are uncorrelated and that  $\langle \delta_2^2 \rangle = \langle \delta_2 \rangle^2$  and  $\langle v_2^4 \rangle = \langle v_2^2 \rangle^2$ . This means that we neglected the event by event fluctuations in  $v_2$  and  $\delta_2$ . The effect of the fluctuations on  $v_2$  estimates can be obtained from

$$\begin{aligned} \langle v_2^2 \rangle &= \langle v_2 \rangle^2 + \sigma^2 \\ \langle v_2^4 \rangle &= \langle v_2 \rangle^4 + 6\sigma^2 \langle v_2 \rangle^2 \\ \langle v_2^6 \rangle &= \langle v_2 \rangle^6 + 15\sigma^2 \langle v_2 \rangle^4 \end{aligned} \quad (26)$$

If we now neglect the non-flow terms we get

$$\begin{aligned} v_2\{2\} &= \sqrt{\langle v_2^2 \rangle} = \sqrt{\langle e^{2i(\phi_1 - \phi_2)} \rangle} \\ v_2\{4\} &= \sqrt[4]{2\langle v_2^2 \rangle^2 - \langle v_2^4 \rangle} \\ v_2\{6\} &= \sqrt[6]{\frac{1}{4}(\langle v_2^6 \rangle - 9\langle v_2^2 \rangle \langle v_2^4 \rangle + 12\langle v_2^2 \rangle^3)} \end{aligned} \quad (27)$$

If we assume that  $\sigma \ll \langle v \rangle$  then up to the order of  $\sigma^2$  we get

$$\begin{aligned}v_2\{2\} &= \langle v_2 \rangle + \frac{1}{2} \frac{\sigma^2}{\langle v_2 \rangle} \\v_2\{4\} &= \langle v_2 \rangle - \frac{1}{2} \frac{\sigma^2}{\langle v_2 \rangle} \\v_2\{6\} &= \langle v_2 \rangle - \frac{1}{2} \frac{\sigma^2}{\langle v_2 \rangle}\end{aligned}\tag{28}$$

So we see that the difference between  $v_2[2]$  and  $v_2[4]$  is sensitive to non-flow and fluctuations. [13]

Using this we can indirectly get an estimate of elliptic flow  $v_2$ .

## 2.4 The event plane method

The event plane (EP) method is based on reconstructing the symmetry plane of a collision; the event plane  $\Psi_{EP}$ . In this method we measure momentum space anisotropy with respect to the event plane  $\Psi_{EP}$ . The event plane is estimated using the same Q-vector as was used for the SP method and was defined as

$$Q_n = \sum_{i=1}^M e^{in\phi_i} \quad (29)$$

where M is the multiplicity of the event and  $\phi_i$  is the azimuthal angle of an outgoing track in the laboratory frame.

The Q-vector can be rewritten as

$$Q_n = \sum_{i=1}^M e^{in\phi_i} = |Q_n| e^{in\Psi_{Q_n}} = Q_{n,x} + iQ_{n,y} \quad (30)$$

where

$$\begin{aligned} Q_{n,x} &= |Q_n| \cos n\Psi_{Q_n} \\ Q_{n,y} &= |Q_n| \sin n\Psi_{Q_n} \end{aligned} \quad (31)$$

where  $\Psi_{Q_n}$  is the azimuthal angle of the Q-vector, which corresponds to the orientation of the event plane  $\Psi_{EP}$ .

The event plane  $\Psi_{EP}$  can now be determined as

$$\Psi_{EP} = \frac{1}{2} \arctan 2(Q_{2,y}, Q_{2,x}) \quad (32)$$

The  $\arctan 2(y, x)$  gives the arctangent of  $\frac{y}{x}$  in the interval  $(-\pi, \pi]$  with

$$\begin{aligned} if(x \neq 0 \wedge y \neq 0); \arctan 2(y, x) &= \tan^{-1}\left(\frac{y}{x}\right) \\ if(x = 0); \arctan 2(y, x) &= 0 \\ if(x > 0 \wedge y = 0); \arctan 2(y, x) &= \frac{\pi}{2} \\ if(x < 0 \wedge y = 0); \arctan 2(y, x) &= -\frac{\pi}{2} \end{aligned} \quad (33)$$

For the observed flow we now average over all events such that

$$v_n^{obs} = \langle \cos(n[\phi - \Psi_{EP}]) \rangle \quad (34)$$

Since each event has a finite multiplicity the event plane can never be reconstructed perfectly. To correct for this effect the observed flow is divided by the event plane resolution  $R$ . The event plane resolution is given by the correlation of the event plane with the symmetry plane:

$$R = \langle \cos(n[\Psi_{EP} - \Psi_n]) \rangle \quad (35)$$

which gives

$$\begin{aligned} v_n &= \langle e^{n[\phi - \Psi_n]} \rangle = \langle e^{n[\phi - \Psi_{EP}] - n[\Psi_{EP} - \Psi_n]} \rangle \\ &= \frac{\langle e^{n[\phi - \Psi_{EP}]} \rangle}{\langle e^{n[\Psi_{EP} - \Psi_n]} \rangle} = \frac{v_n^{obs}}{R} \end{aligned} \quad (36)$$

This resolution correction was introduced because  $\Psi_n$  can not directly be determined experimentally, which means that the resolution correction also can not be determined directly. However we can determine the resolution by using three sub-events of unequal multiplicity or resolution. From the definition of  $R$  we can find that for two sub-events  $a$  and  $b$  we get

$$\begin{aligned} \langle \cos(n[\Psi_{EP}^a - \Psi_{EP}^b]) \rangle &= \langle \cos(n[\Psi_{EP}^a - \Psi_n]) \rangle \langle \cos(n[\Psi_{EP}^b - \Psi_n]) \rangle \\ &= R_n^a R_n^b \end{aligned} \quad (37)$$

If we now include a third sub-event  $c$  we get

$$\begin{aligned} \langle \cos(n[\Psi_{EP}^a - \Psi_{EP}^c]) \rangle &= \langle \cos(n[\Psi_{EP}^a - \Psi_n]) \rangle \langle \cos(n[\Psi_{EP}^c - \Psi_n]) \rangle \\ &= R_n^a R_n^c \\ \langle \cos(n[\Psi_{EP}^b - \Psi_{EP}^c]) \rangle &= \langle \cos(n[\Psi_{EP}^b - \Psi_n]) \rangle \langle \cos(n[\Psi_{EP}^c - \Psi_n]) \rangle \\ &= R_n^b R_n^c \end{aligned} \quad (38)$$

From this we get the three sub-event resolution corrections:

$$\begin{aligned} R_n^a = \langle \cos(n[\Psi_{EP}^a - \Psi_n]) \rangle &= \sqrt{\frac{\langle \cos[n(\Psi_{EP}^a - \Psi_{EP}^b)] \rangle \langle \cos[n(\Psi_{EP}^a - \Psi_{EP}^c)] \rangle}{\langle \cos[n(\Psi_{EP}^b - \Psi_{EP}^c)] \rangle}} \\ R_n^b = \langle \cos(n[\Psi_{EP}^b - \Psi_n]) \rangle &= \sqrt{\frac{\langle \cos[n(\Psi_{EP}^a - \Psi_{EP}^b)] \rangle \langle \cos[n(\Psi_{EP}^b - \Psi_{EP}^c)] \rangle}{\langle \cos[n(\Psi_{EP}^a - \Psi_{EP}^c)] \rangle}} \\ R_n^c = \langle \cos(n[\Psi_{EP}^c - \Psi_n]) \rangle &= \sqrt{\frac{\langle \cos[n(\Psi_{EP}^a - \Psi_{EP}^c)] \rangle \langle \cos[n(\Psi_{EP}^b - \Psi_{EP}^c)] \rangle}{\langle \cos[n(\Psi_{EP}^a - \Psi_{EP}^b)] \rangle}} \end{aligned} \quad (39)$$

With this method it is not possible to differentiate between the true anisotropic flow and contributions from flow fluctuations and non-flow contributions. The non-flow contributions can be reduced significantly by using multi-particle correlation.

### 2.4.1 $\phi - \Psi$ method for elliptic flow

The  $\phi - \Psi$  method is based on the event plane method. This method is based on extracting the raw yield of the electrons in different  $\Delta\phi = \phi - \Psi$  bins. From the signal distributions the raw yield  $\frac{dN}{d[\phi - \Psi_2]}$  is extracted, where  $\Psi_2$  is defined as

$$\Psi_2^i = \frac{1}{2} \arctan 2 \left( \sum_{i=0}^M \sin(2\phi), \sum_{i=0}^M \cos(2\phi) \right) \quad (40)$$

where  $M$  is the multiplicity of the reference particles.

The extracted yield is fitted with the following function:

$$\frac{dN}{d[\phi - \Psi_2]} = N_0 \times (1 + 2v_2^{obs} \cos[2(\phi - \Psi_2)]) \quad (41)$$

In this function  $N_0$  and  $v_2^{obs}$  are free parameters.

From the yield distribution fit we extract  $v_2^{obs}$ . From this point we continue in the same way as for the event plane method and correct for the resolution of the detector.

$$v_2^a = \frac{v_2^{obs}}{R_n^a} \quad (42)$$

with the event plane resolution  $R_n^a$ .

A more detailed explanation of how this method is applied in this study can be found in section 4.5

### 3 Introduction to the detector

The ALICE detector consists of central barrel optimised for detecting electrons, hadrons and photons. The central barrel is embedded in a solenoid magnet. The detector also includes a forward muon spectrometer. The pseudo-rapidity region of the detector is  $|\eta| \leq 0.9$ . The detector has a size of  $16 \times 16 \times 26 \text{ m}^3$  and weighs approximately 10000 tonnes.

In figure 7 the ALICE detector is illustrated. To identify inclusive electrons the TPC (Time Projection Chamber) and EMCAL (Electro magnetic calorimeter) are used. For calculating  $\phi - \Psi$  and the multiplicity the VZERO (V0) was used. To determine the vertex the TRK and SPD were used and to determine the centralities the TRK and VZERO were used. A more detailed explanation about the sub-detectors used can be found below.

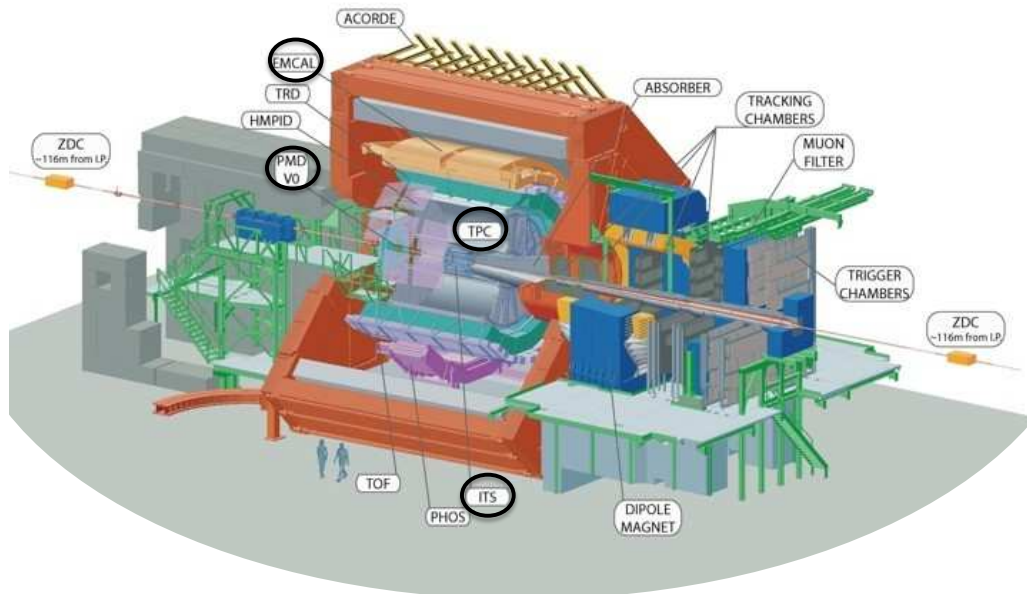


Figure 7: The alice detector

**ITS** The Inner Tracking System (ITS) consists of six layers which includes a Silicon Pixel Detector (SPD), a Silicon Drift Detector (SDD) and a Silicon Strip Detector (SSD). The ITS covers a pseudo-rapidity region of  $|\eta| = 0.9$ . This subdetector can be used for many purposes. In this study it is mainly used for locating the primary interaction vertex and tracking. The ITS could also be used for particle identification (PID) based on  $\frac{dE}{dx}$  measurements in the SSD and SDD however due to the  $p_T$  region in which ITS PID is reliable it is not used in this study. ITS PID is done from 1 GeV/c and in the lowest range it is not yet reliable, which is the range used in this study.

**TPC** The TPC is a cylindrical, gas filled detector, optimised for momentum measurements of charged- particles. It covers a  $p_T$  range of  $0.1[GeV/c] \leq p_T \leq 100[GeV/c]$  and a pseudo-rapidity range of  $|\eta| \leq 0.9$  for tracks with full track length and  $|\eta| \approx 1.5$  for tracks which pass through part of the detector. The TPC can measure up to 159 clusters. Tracks with full track length are reconstructed using all the available 159 clusters. If the number of used clusters used in track reconstruction is lower the pseudo-rapidity range increases, however these tracks are reconstructed with a lower resolution than the resolution of full length tracks.

Momentum measurements in combination with energy loss per distance traveled by a particle measurements,  $\frac{dE}{dx}$  are used for flow analysis of identified particles. Energy loss per distance traveled by a particle through a specific material is described by the Bethe-Bloch formula:

$$\frac{dE}{dx} = \frac{4\pi}{m_e c^2} \frac{n z^2}{\beta^2} \left(\frac{e^2}{4\pi\epsilon_0}\right)^2 \left[\ln\left(\frac{2m_e c^2 \beta^2}{I(1-\beta^2)}\right) - \beta^2\right] \quad (43)$$

where  $\beta$  equals  $v/c$ ,  $v$  is velocity of the particle,  $c$  is the speed of light,  $E$  is the energy of the particle,  $x$  is the distance traveled by the particle,  $m_e$  is the rest mass of the electron,  $n$  is the electron density of the target,  $z$  is the particle charge,  $e$  is the charge of the electron,  $\epsilon_0$  is the vacuum permittivity and  $I$  the mean excitation potential of the target.

The TPC is calibrated in order to describe energy loss per distance traveled with a parameterization of the Bethe-Bloch formula. By combining momentum- and energy loss measurements the particles can be identified. In this analysis particle tracks are reconstructed using global tracks, which are tracks reconstructed using both TPC and ITS signals. Particles are also identified by using the TPCs signal. In addition to particle tracking and identification the TPC is used to estimate collision centrality based on charged particle multiplicity, to estimate the event plane ( $\Psi_{EP}$ ) and to determine E/p.

**EMCal** The electromagnetic calorimeter (EMCal) detector is used in this study for particle identification (PID) and to determine the energy for the  $E/p$  distribution. The electromagnetic calorimeter is located at 4.6m from the interaction vertex and is made of dense scintillating crystals. A second electromagnetic calorimeter consist of several modules made of alternating layers of 1.44 mm Pb and 1.76 mm polystyrene. This detector can also be used for triggering on electrons.

**VZERO** The VZERO detector is used in this study for centrality determination and to estimate event plane ( $\Psi_{EP}$ ). It consists of two arrays of 32 scintillator counters, VZERO-A and VZERO-C, placed on either side of the interaction point. VZERO-A spans  $2.8 < \eta < 5.1$  and VZERO-C spans  $-3.7 < \eta < -1.7$  and they have full azimuthal coverage. The total VZERO detector has a fixed multiplicity of 64. When the signal strength is weighted each counter gives an estimate of the number of charged tracks passing through the detector. Since the relation between registered VZERO particles and primary particles is monotone the VZERO signal can be used for centrality determination.

### 3.1 The ALIROOT framework

For this thesis the analysis is done using the AliROOT framework. This framework was developed for the ALICE experiment as an extension of the ROOT framework and is based on the c programming language. The analysis was done using different analysis tags from v5-04-22-AN until v5-05-35-AN. The electron identification was done with the software package of the Heavy Flavour Electron working group which can be found in the PWGHF/hfe directory.

The event selection and centrality determination are done with the AliPhysicsSelection and AliCentralitySelectionTask classes. The event plane is reconstructed using the AliVZEROEPSelectionTask class.

The flow analysis methods done for comparison (SP, QC and EP) are done using the Flow-Pachage PWGCF/FLOW. The elliptic flow analysis for electrons is done using AliAnalysisTaskFlowTPCEMCalQCSP.h AliAnalysisTaskFlowTPCEMCalQCSP.cxx and AddTaskFlowTPCEMCalQCSP.C.



## 4 Inclusive electron $v_2$

### 4.1 Event selection

The data analysed in this thesis was collected in 2011 from Pb-Pb collisions at a center-of-mass energy of  $\sqrt{s_{NN}} = 2.76$  TeV. For the analysis AOD115 productions corresponding to LHC11h/pass2 were used. The analysis is performed for events with a centrality between 20% and 40%. The centrality is determined using the VZERO multiplicity. In total around  $6 \times 10^6$  events were analysed.

The list of runs used for this analysis is the following:

170593, 170572, 170388, 170387, 170315, 170313, 170312, 170311, 170309, 170308, 170306, 170270, 170269, 170268, 170230, 170228, 170207, 170204, 170203, 170193, 170163, 170159, 170155, 170091, 170089, 170088, 170085, 170084, 170083, 170081, 170040, 170027, 169859, 169858, 169855, 169846, 169838, 169837, 169835, 169591, 169590, 169588, 169587, 169586, 169557, 169555, 169554, 169553, 169550, 169515, 169512, 169506, 169504, 169498, 169475, 169420, 169419, 169418, 169417, 169415, 169411, 169238, 169167, 169160, 169156, 169148, 169145, 169144, 169138, 169099, 169094, 169091, 169045, 169044, 169040, 169035, 168992, 168988, 168826, 168777, 168514, 168512, 168511, 168467, 168464, 168460, 168458, 168362, 168361, 168342, 168341, 168325, 168322, 168311, 168310, 167988, 167987.

On the data we apply a cut that the number of tracks in an event has to be greater than two to reject bad events. After that a cut is applied on the vertex distribution where  $|z| < 10$ . On the vertex distribution we also require that the absolute difference between the TRK and SPD vertexes less is than 0.5 cm. This is done to help remove events affected from pile up. Pile up events are events coming either from another Pb-Pb collisions or Pb-Pb collisions in a previous bunch. Events coming from another Pb-Pb collision can be misidentified because tracks might come close or through tracks of events coming from the studied collision. Events coming from a previous bunch might be misidentified since the TPC is slow and might still be recording from the previous collision. The vertex distribution after these cuts is illustrated in figure 8.

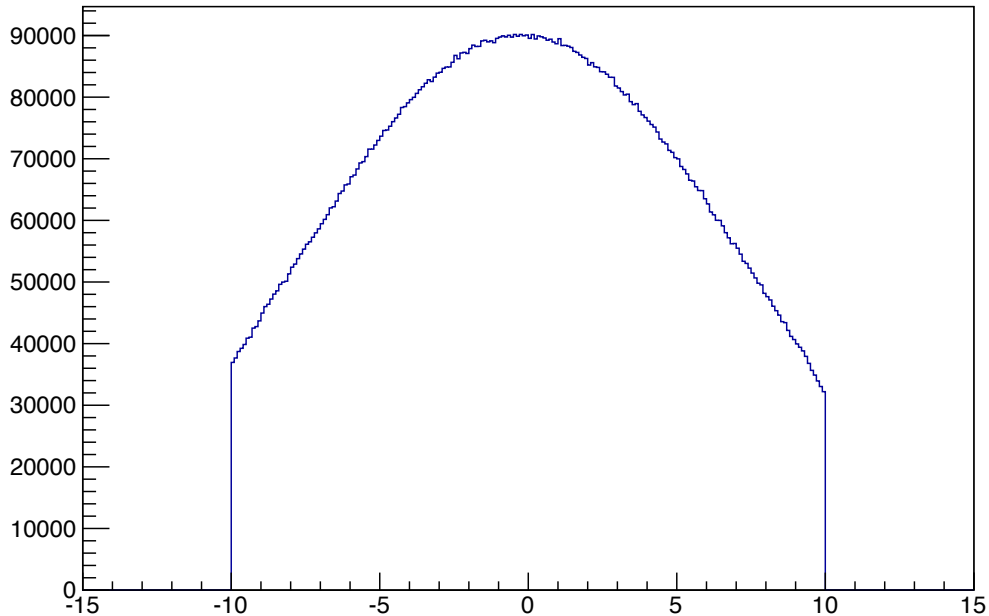


Figure 8: vertex distribution

The absolute difference between the TRK and VZERO centralities<sup>4</sup> is required to be less than 5%. This cut is also made to remove events effected from pile up. The centrality distribution after this cut and selecting a centrality between 20% and 40% is shown in figure 9.

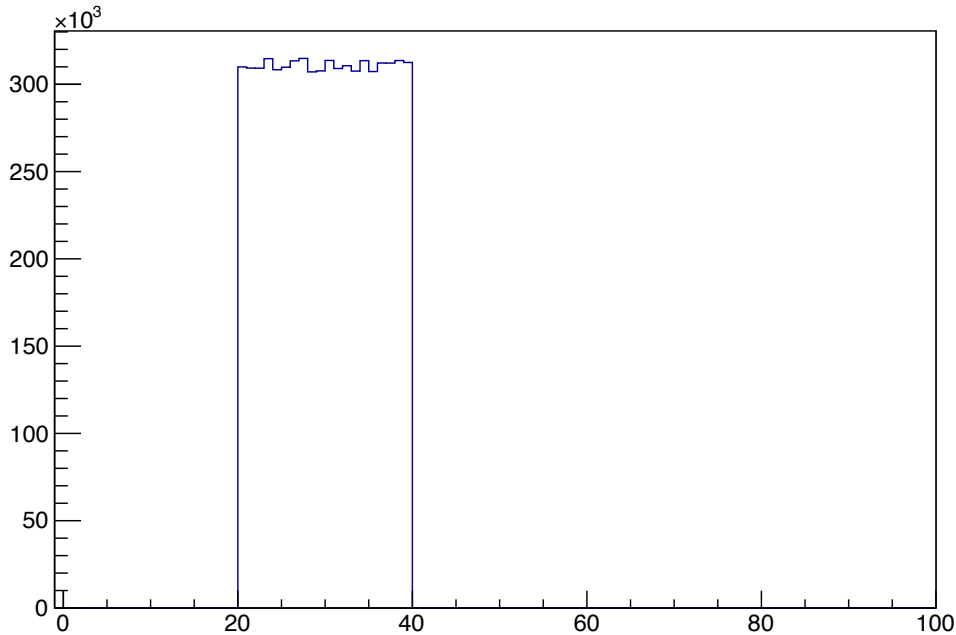


Figure 9: centrality pass

Another cut to help remove the events affected from pile up is on the multiplicity distribution;

The correlation between the global track multiplicity<sup>5</sup> and TPC track multiplicity is expected to be linear. However if the events are affected by outliers or pile up this might not be the case. In figure 10 it is seen that the correlation between the global and TPC track multiplicities is not linear. To reject the non-linear events from the data we project slices along the y axis of this correlation plot. Each of these slices is fitted with a gaussian function. The mean (left side figure 11) and sigma (right side figure 11) of that gaussian fit are fitted with a linear function. From these two linear fits we determine

<sup>4</sup>The centrality of a collision is a measure of the events impact parameter.

<sup>5</sup>(Charged particle) multiplicity is the number of (charged) particles which is observed in a detector.

$mean \pm 3 \times sigma$  and reject events outside this range (indicated with red lines in figure 10).

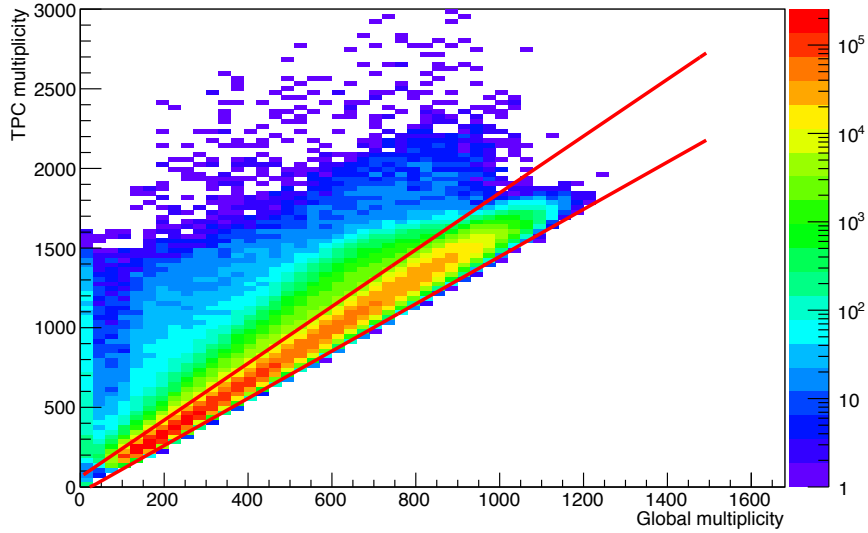


Figure 10: Multiplicity Fit

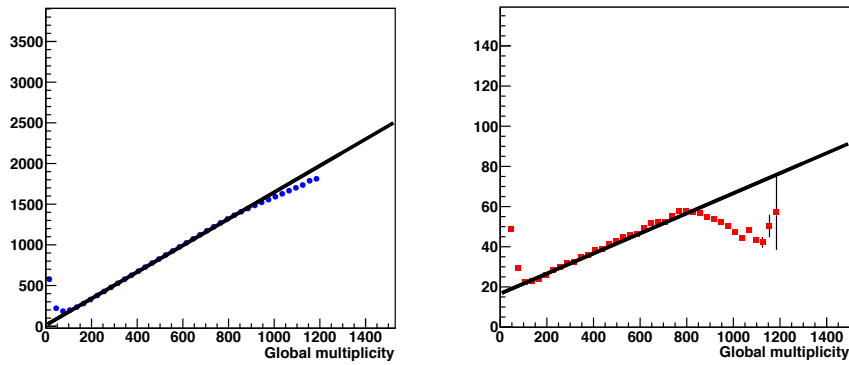


Figure 11: Multiplicity Fit. Mean on the left, sigma on the right.

All these cuts are summarised in table 1.

type	requirement
trigger	kSemiCentral
# of tracks in an event	$> 2$
centrality	20% - 40%
vertex $ z $	$< 10$ cm
Pile up cuts	
centrality( $ VZERO - TRK $ )	$< 5\%$
vertex( $( SPD - TRK )$ )	$< 0.5$ cm
correlation global and TPC track multiplicity	linearised

Table 1: Event selection cuts

A check is done on the VZEROA and VZEROC event plane distributions. We want these distributions to be flat because we integrate over these distributions when we determine the event plane resolution. In figures 12 and figure 13 we see that these distributions are indeed approximately flat. Also for the centrality which was shown in figure 9 we notice that the distribution is flat which is needed when we integrate  $v_2$  over the centrality.

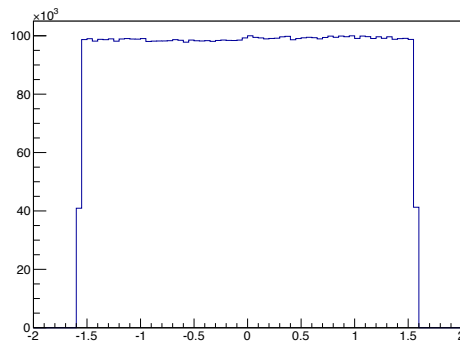


Figure 12: VZEROA event plane distribution

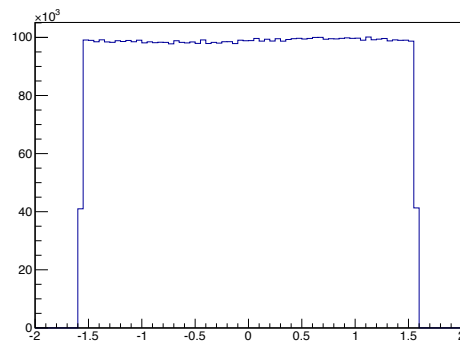


Figure 13: VZEROC event plane distribution

## 4.2 Track selection

We require a hit in both SPD layers. This is done to reject electrons that are coming from  $\gamma$  conversion in the detector instead of directly from weak decay.

Some particles scatter inside the ALICE detector. After these particles have scattered they are often misidentified as new tracks. These kick candidates are therefore also rejected.

If we have more points to construct a track with we get a more precise track reconstruction. For this reason we require a minimum number of clusters in the TPC and the ITS. To improve the track reconstruction we require a minimum ration of TPC clusters and a maximal  $\chi^2$  per TPC cluster.

Finally we require that the tracks are refitted in the ITS and TPC. By doing this we improve the resolution on each single track. For the ITS only a minimum of 3 clusters is required therefore the refitting requirement on the ITS provides a considerable boost to the rejection of tracks from pile up.

The track selection for electron candidates are summarised in table 2.

type	range
$p_T$ [GeV/c]	[1,10]
$\eta$	[-0.7,0.7]
type	requirement
AliAODTrack::kTrkGlobalNoDCA	Bit 4
hit SPD layers	both
reject kink candidates	yes
min # TPC clusters	100
min # ITS clusters	3
min ration of TPC clusters	0.6
max $\chi^2$ per TPC cluster	3.5
ITS and TPC refit	yes

Table 2: Track selection cuts for electron candidates

### 4.3 Particle identification and cut optimisation

After these event and track selection we can continue to particle identification of inclusive electrons. For this task we use the TPC and EMCal detectors. For the TPC the particle identification is based on the energy loss ( $dE/dx$ ) in de gas of the detector. The energy loss is expressed as a deviation from the parametrized electron Bethe-Bloch line divided by the energy loss resolution. This is called TPC  $n\sigma$ . This is illustrated in figure 14. To select the inclusive electrons we require  $-1 < N\sigma < 3$ . These values are chosen to select a high electron purity.

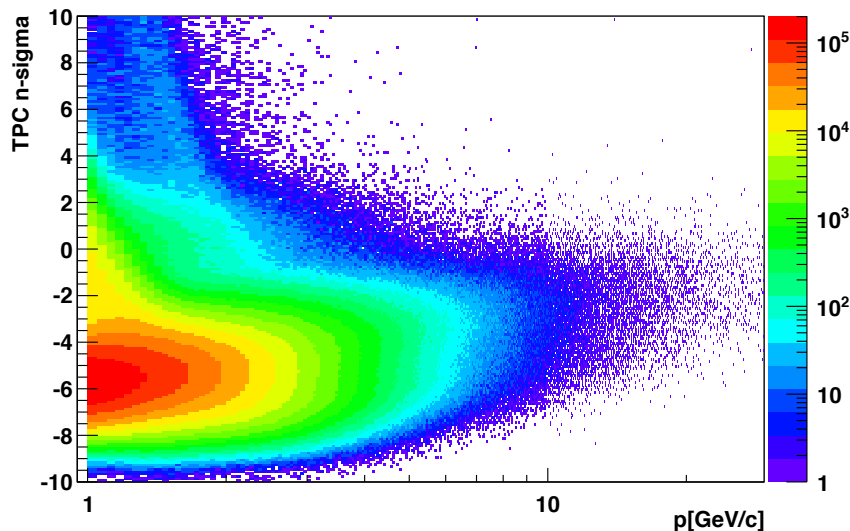


Figure 14: TPC  $n$ -sigma distribution before cut

For the EMCal detector the particle identification is based on the  $E/p$  distribution. Where the energy  $E$  is coming from the EMCal cluster and the momentum  $p$  if coming from the TPC. For electrons this ratio should be unity since the mass of the electron is so small that it can be neglected. In figure 15 the  $E/p$  distribution after the TPC  $N\sigma$  cut is shown. After the hadron contamination has been subtracted, tracks with  $E/p$  between 0.8 and 1.2 are selected as electrons<sup>6</sup>.

<sup>6</sup>The figure shows the  $E/p$  distribution before any shower shape cut was applied. However electron are selected in this  $E/p$  range after the shower shape cut is applied



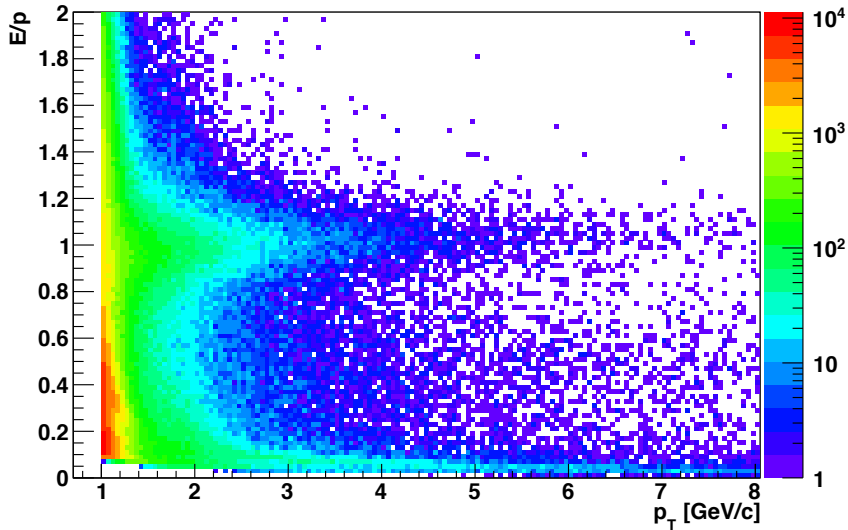


Figure 15: inclusive electron projection,  $E/p$  distribution

The last cut applied is on the shower shape. Here we cut on the dimension of the two axes of the transversal projection of the shower in the electromagnetic calorimeter and on its dispersion. The long axis is called M02 and the short axis is called M20. The two axes are indicated in figure 16. In figure 17 and figure 18 the M20 and M02 distributions as a function of  $E/p$  are shown before the cuts are made.

In figures 20 and 19 The M02 and M20 distributions are shown in the area which we select. The shower shape cut is an important cut since it cuts a lot. For this reason this cut is optimised by studying different sets of cuts.

Figure 21 shows the  $E/p$  distribution for different shower shape cuts. Based on this figure we decided to use the regular cut (black) since the contamination is visibly reduced for this cut. In table 3 the specifics of the different cuts are shown.

The shower shape cuts and the cuts on TPC  $N\sigma$  and the  $E/p$  distribution are summarised in table 4.

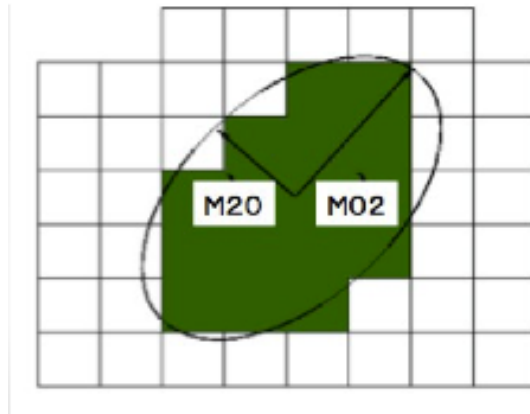


Figure 16: shower shape cut

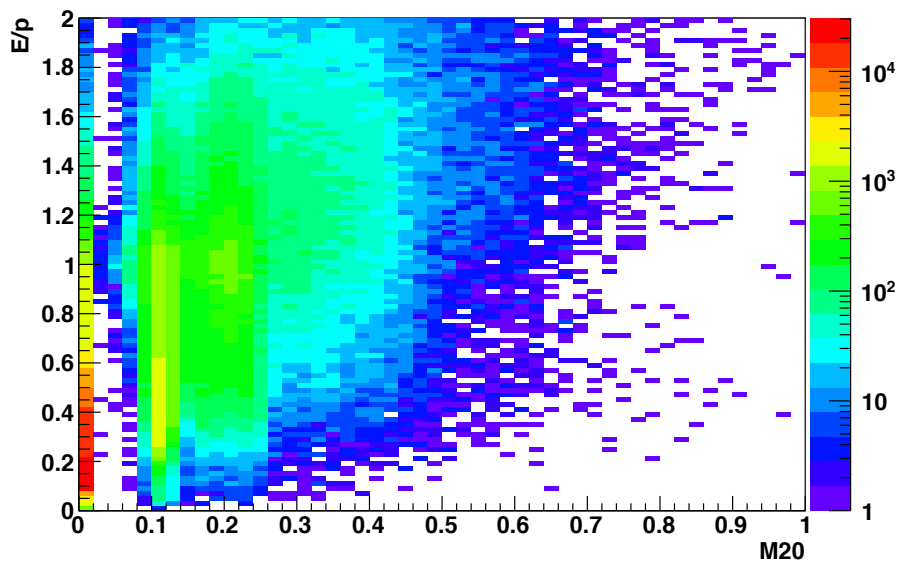


Figure 17: M20 distribution before cut

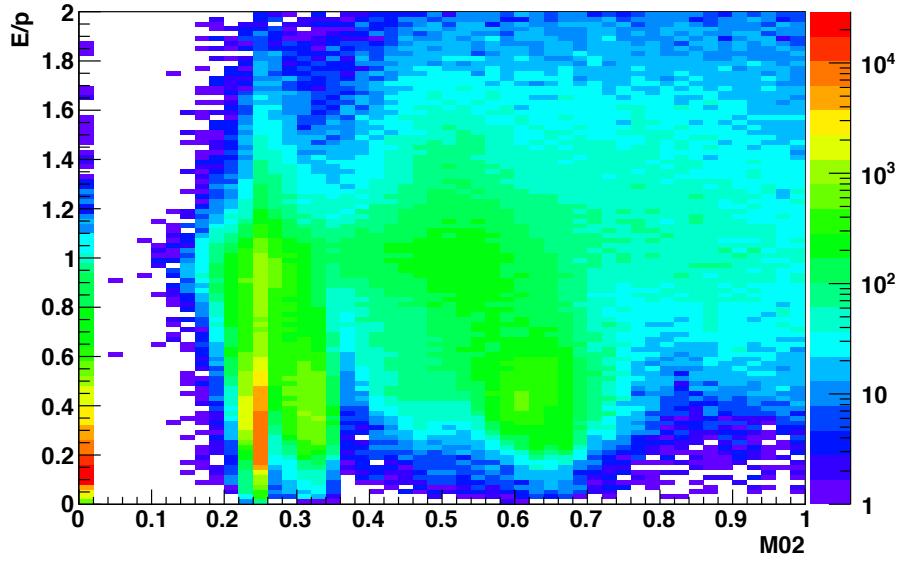


Figure 18: M02 distribution before cut

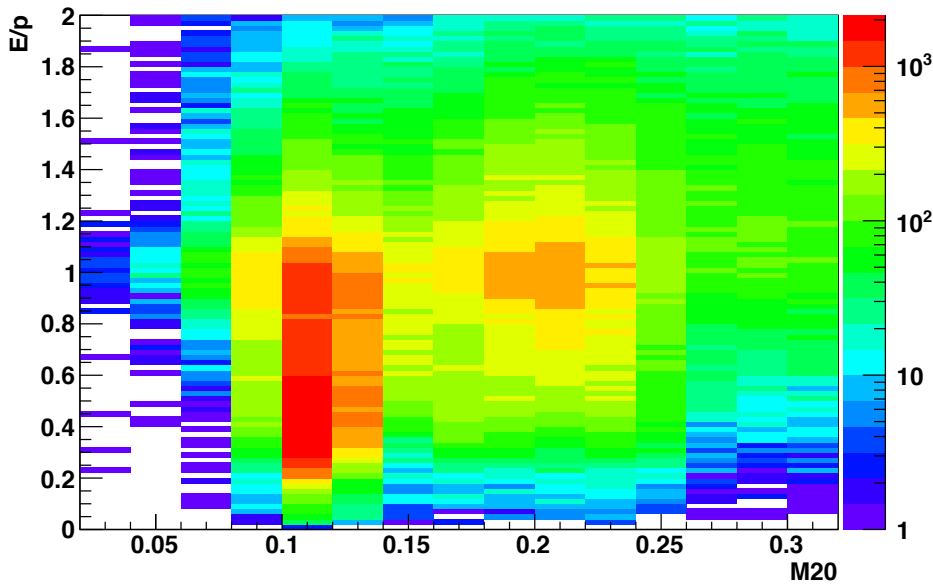


Figure 19: M20 distribution in the selection range

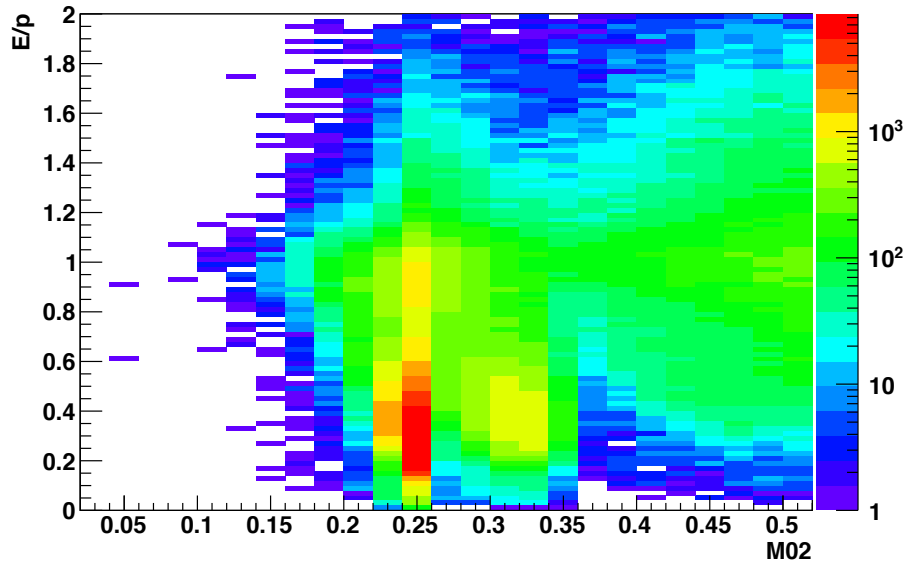


Figure 20: M02 distribution in the selection range

Regular cut	
M20 (short axis)	[0.03,0.3]
M02 (long axis)	[0.03,0.5]
dispersion	< 1
Other cut	
M20 (short axis)	[0.0,0.2]
M02 (long axis)	[0.0,0.5]
dispersion	< 1

Table 3: Different shower shape cuts

type	requirement
$N\sigma$	[-1,3]
E/p	[0.8,1.2]
sscuts	
M20 (short axis)	[0.03,0.3]
M02 (long axis)	[0.03,0.5]
dispersion	< 1

Table 4: Electron identification cuts

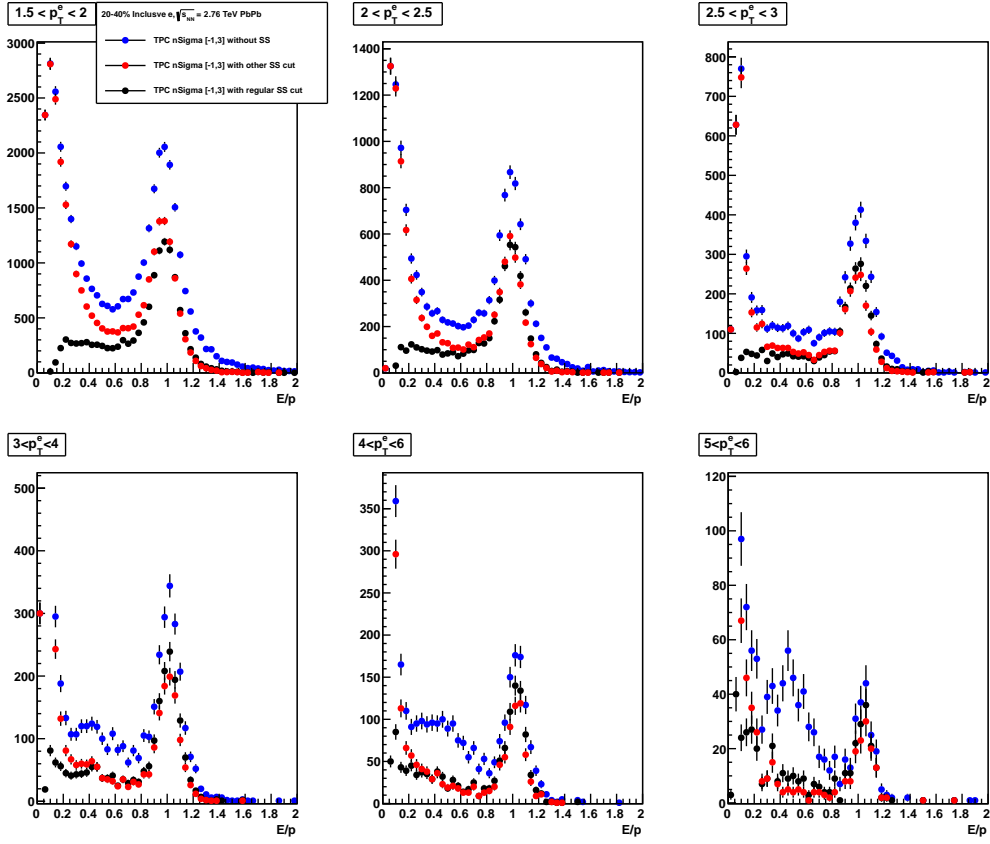


Figure 21: Optimisation of the shower shape cut

#### 4.4 Background estimation

The last step before extracting the yield is to remove the hadron contamination under the electron peak in the  $E/p$  distribution. Two different approaches to remove the background are studied. The first method consists of fitting a gaussian plus second order polynomial to the  $E/p$  distribution and subtract the second order polynomial as background. The other method removes the background based on the data. This data driven method is done by selecting hadrons using the TPC  $n\sigma$  and using that distribution to subtract the background under the electron peak.

We have seen that electrons are selected by cutting on TPC  $N\sigma$  to be in the range  $[-1,3]$ . We now apply a cut on the TPC  $N\sigma$  for hadrons to be in the range  $[-10,-3.5]$ . The selected hadron tracks are then normalised in the lower range of the electron  $E/p$  distribution (in the  $E/p$  range from 0.2 to 0.7). This normalisation is necessary since the number of hadrons selected in the  $[-10,-3.5]$  range is much larger than the number of electrons selected in the  $[-1,3]$  of TPC  $N\sigma$  range.

Figure 22<sup>6</sup> includes a normalised hadron distribution as pink points.

To compare the background subtraction using the fitting routine and the data driven method figure 22<sup>7</sup> is added. This figure gives an example of how the two methods differ in the background reduction.

We see that especially in the range under the electron peak between 0.8 and 1.2, the fitting method seems to overestimate the contamination. At the same time we see that the data driven method describes the background in the side bands better.

We can also see a difference in the purity of the electron sample for these two methods. The purity has been calculated by

$$\frac{\frac{dN_i}{d[\phi-\Psi_2]}}{\frac{dN_{electrons}}{d[\phi-\Psi_2]} + \frac{dN_{hadrons}}{d[\phi-\Psi_2]}} \quad (44)$$

where the  $i$  can be either electrons for the electron purity or hadrons for the hadron purity.

---

<sup>7</sup>Other bins can be found in the appendix

The difference in purity is shown in figure 23. From this plot it is clear that the data driven method has a higher purity than the fitting routine. Which is as we expected since we already concluded that the data driven method describes the background better. The shape of the background distribution together with the purity suggest that fitting a second order polynomial over-estimates the background. The fitting routine has been used a systematic study on extracting  $v_2$ .

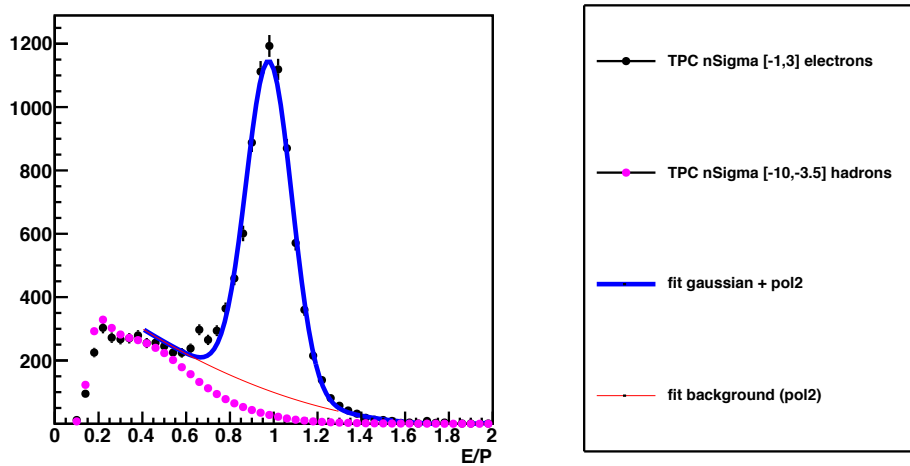


Figure 22: comparing background reduction,  $E/p \ 1.5 < p_T < 2$ ,  $\phi$  integrated

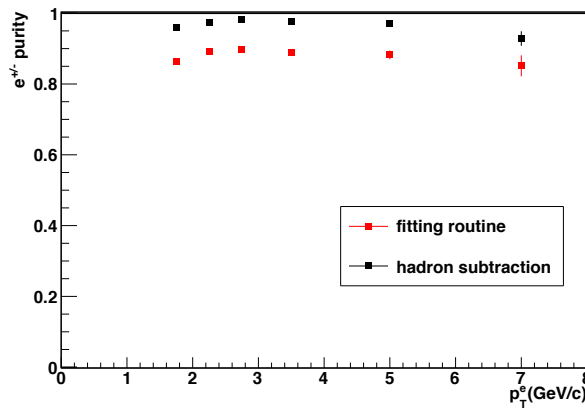


Figure 23: purity comparison of electrons

For the continuing study we decided to use the data driven method to remove the background.

### 4.5 $\phi - \Psi$ method

From the E/p distributions after the background has been subtracted we extract the raw yield  $\frac{dN}{d[\phi - \Psi_2]}$  where  $\Psi_2$  is defined as

$$\Psi_2^i = \frac{1}{2} \arctan 2 \left( \sum_{i=0}^M \sin(2\phi), \sum_{i=0}^M \cos(2\phi) \right) \quad (45)$$

where M is the multiplicity of the reference particles.

For each of our original  $p_T$  bins we now plot the yield extracted for each  $\Delta\phi$  bin. This gives a yield distribution for all  $p_T$  bins. We can now fit the following function to the yield distribution per  $p_T$  bin:

$$\frac{dN}{d[\phi - \Psi_2]} = N_0 \times (1 + 2v_2^{obs} \cos[2(\phi - \Psi_2)]) \quad (46)$$

In this function  $N_0$  and  $v_2^{obs}$  are free parameters.

From the yield distribution fit we extract  $v_2^{obs}$ . The observed elliptic flow,  $v_2^{obs}$ , then needs to be corrected for the resolution of the detector. In this study the three sub-events are the resolutions coming from the VZERO-A, VZERO-C and TPC detectors.

$$v_2^a = \frac{v_2^{obs}}{R_n^a} \quad (47)$$

with the event plane resolutions:

$$\begin{aligned} R_n^a &= \langle \cos(n[\Psi_{EP}^a - \Psi_n]) \rangle = \sqrt{\frac{\langle \cos[n(\Psi_{EP}^a - \Psi_{EP}^b)] \rangle \langle \cos[n(\Psi_{EP}^a - \Psi_{EP}^c)] \rangle}{\langle \cos[n(\Psi_{EP}^b - \Psi_{EP}^c)] \rangle}} \\ R_n^b &= \langle \cos(n[\Psi_{EP}^b - \Psi_n]) \rangle = \sqrt{\frac{\langle \cos[n(\Psi_{EP}^a - \Psi_{EP}^b)] \rangle \langle \cos[n(\Psi_{EP}^b - \Psi_{EP}^c)] \rangle}{\langle \cos[n(\Psi_{EP}^a - \Psi_{EP}^c)] \rangle}} \\ R_n^c &= \langle \cos(n[\Psi_{EP}^c - \Psi_n]) \rangle = \sqrt{\frac{\langle \cos[n(\Psi_{EP}^a - \Psi_{EP}^c)] \rangle \langle \cos[n(\Psi_{EP}^b - \Psi_{EP}^c)] \rangle}{\langle \cos[n(\Psi_{EP}^a - \Psi_{EP}^b)] \rangle}} \end{aligned} \quad (48)$$

Where  $a$ ,  $b$  and  $c$  are the three detectors.



The E/p distributions are divided in  $p_T$  bins. Of each E/p distribution slices are made for different  $\Delta\phi = \phi - \Psi_2$ .

After the hadron E/p distribution has been normalised we subtract the hadron E/p distribution from the electron E/p distribution to get the electron yield.

We can now directly extract the yield of the electrons by integrating the histogram of each electron E/p distribution; (Different ways of extraction the electron yield in the systematics chapter.)

$$\int_{0.8}^{1.2} x_i dx \quad (49)$$

This gives one point for each  $\Delta\phi$  bin within each  $p_T$  bin. For each  $p_T$  bin we now have a yield distribution depended on  $\Delta\phi$ . To these points we then fit the following function;

$$\frac{dN}{d[\Delta\phi]} = N_0(1 + 2v_2^{obs} \cos(2\Delta\phi)) \quad (50)$$

Where  $N_0$  and  $v_2^{obs}$  are the free parameters. The extracted yield is shown in figure 24<sup>8</sup>.

From the  $\frac{dN}{d[\Delta\phi]}$  fit we now extract  $v_2^{obs}$  for each  $p_T$  bin for the V0A and V0C detectors. These are is plotted in figure 25.

The observed  $v_2$  is then corrected for the event plane resolutions (equation 48). The results from VZERO-A and VZERO-C are then combined in the following way;

$$v_2^{fin} = \frac{v_2^{V0A}/(\sigma v_2^{V0A})^2 + v_2^{V0C}/(\sigma v_2^{V0C})^2}{1/(\sigma v_2^{V0A})^2 + 1/(\sigma v_2^{V0C})^2} \quad (51)$$

Where the errors are propagated assuming that they are uncorrelated using;

$$\sigma v_2^{fin} = \sqrt{\frac{1}{1/(\sigma v_2^{V0A})^2 + 1/(\sigma v_2^{V0C})^2}} \quad (52)$$

The final  $v_2$  for the VZERO-A and VZERO-C detectors as well as the combined  $v_2$  are shown in figure 26.

<sup>8</sup>Other bins can be found in the appendix

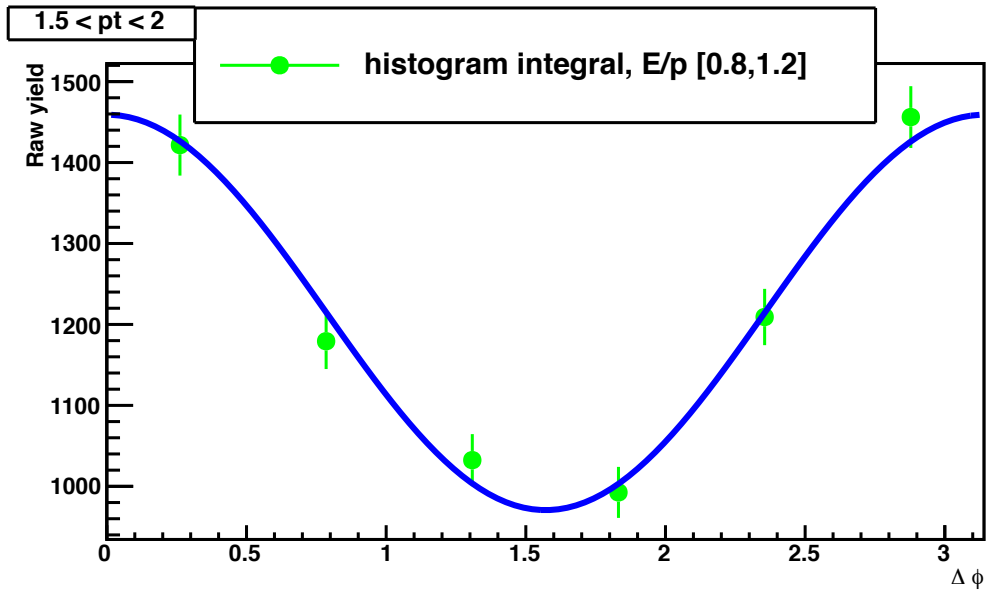


Figure 24: Raw Yield

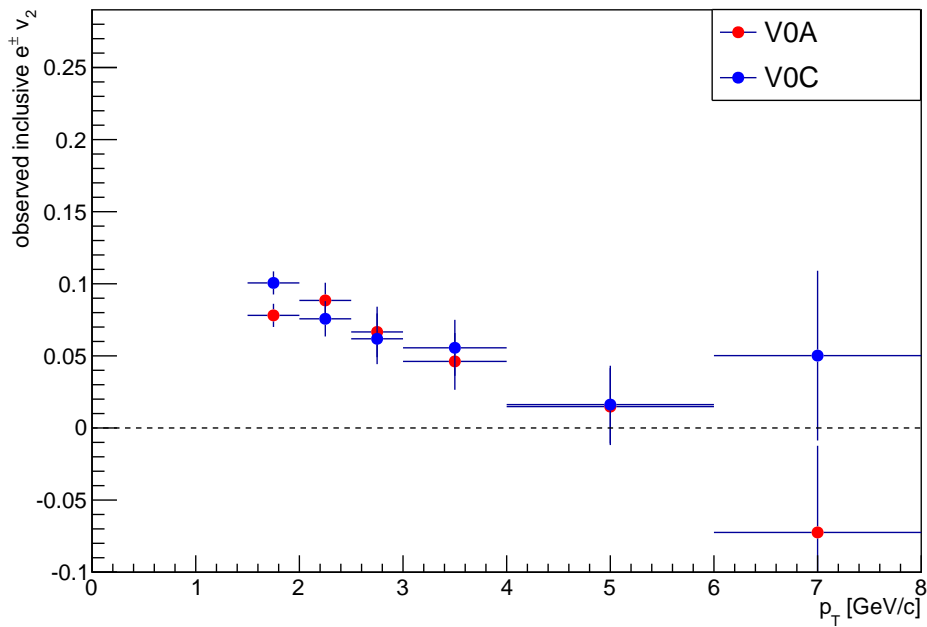
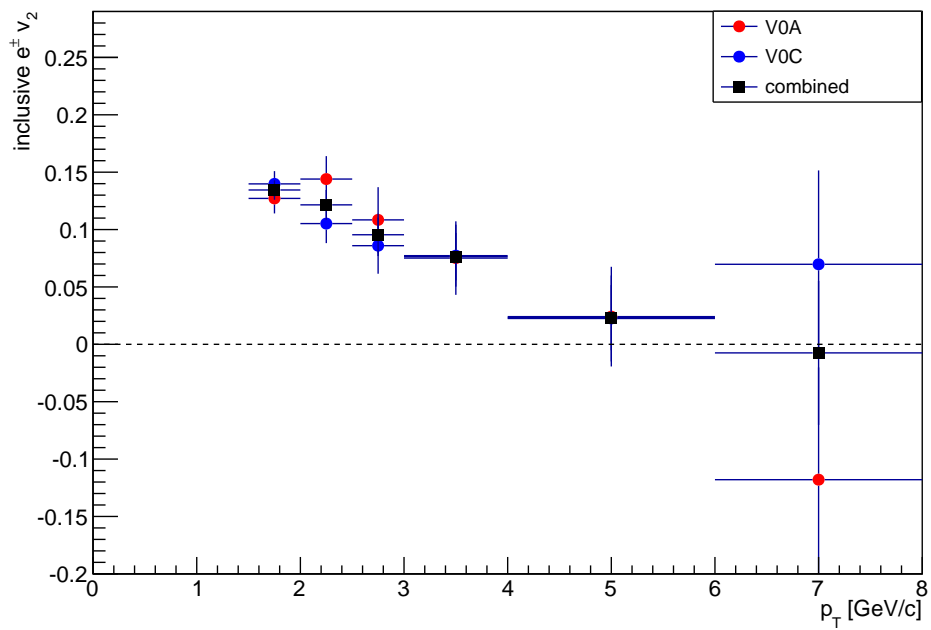


Figure 25:  $v_2$  observed

Figure 26: final  $v_2$

## 4.6 Results

In figure 26 the final result for the elliptic flow has been shown.

We have done a cross check on determining the elliptic flow of inclusive electrons where we remove the contamination at the yield level. This check is conducted by comparing the  $\phi - \Psi$  method with the EP-VO, SP-TPC, SP-VO, QC and the ALICE performance measurement. The comparison for  $v_2$  for all methods is shown in figure 27. We see that all methods are comparable within the error bars. This implies that the effect of contamination is not viable in the other methods.

We see that the methods are less comparable in the two highest  $p_T$  bins ( $4 < p_T < 6$  and  $6 < p_T < 8$ ). This can be explained because of limited available statistics at the moment this study was conducted. Therefore these points are subjected to larger statistical fluctuations which also gives bigger error bars.

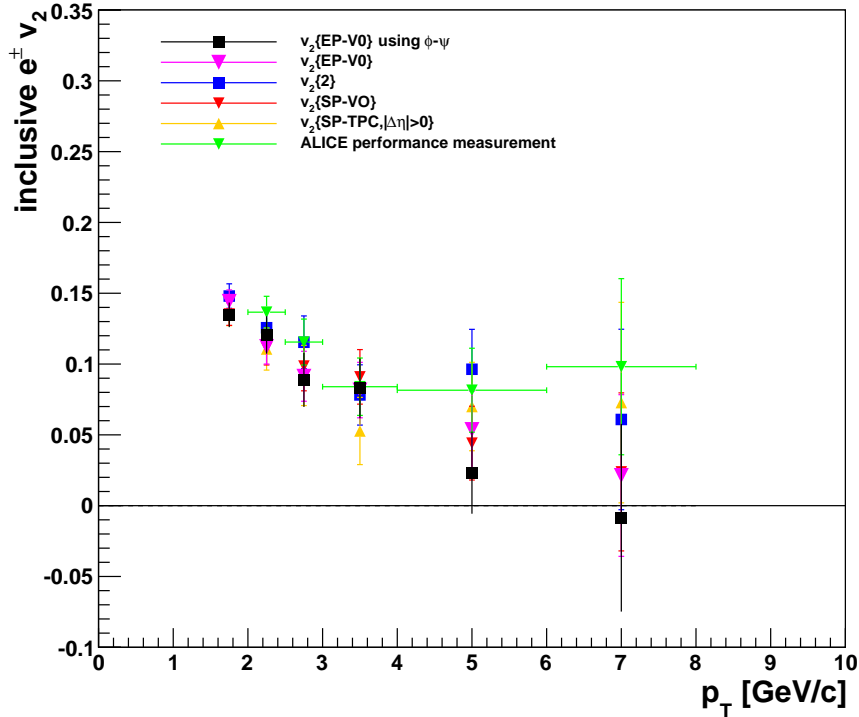


Figure 27: method comparison for  $v_2$  of inclusive electrons

## 5 systematics

The systematics was done by running the the same code but each time with one parameter changed.

As the error for the ratio we consider only the error of the measurement where one parameter has been changed (the error of the default measurement was neglected in order to reduce the statistical fluctuation). This approximation is used because the covariance can not be determined precisely. To calculate the error correctly one should use the following formula;

$$\sigma_{ratio} = \sqrt{\sigma_{regular}^2 + \sigma_{new}^2 + cov} \quad (53)$$

where

$$cov = \frac{\sum_i x_i y_i - n \bar{x} \bar{y}}{(n-1)\sigma_x \sigma_y} \quad (54)$$

with  $x$  the default points and  $y$  the points of the measurement with one parameter changed.

The  $cov$  (covariance) can not be determined because we have only one point in each bin. This causes the  $(n-1)$  to be zero and therefore the denominator to be zero.

In those studies where one of the cuts is a subset of the other the errors were propagated according to the binomial distribution. This is done for the TPC n-sigma study and the study where different shower shape cuts are applied. The error propagation using the binomial distribution is done in the following way;

If B is a subsample of A and we want to compute the fraction  $f = B/A$  then this  $f$  estimates the (binomial) probability  $p$  that a track which passes cut A also passes cut B. The probability of not passing cut B then is  $q = 1 - p$ , since B is a subsample of A so there are only two "options", i.e. success / not-success. The variance from binomial probability on the number of "success" events, i.e. on B, is  $N * p * q$ , where N is the size of your sample A. And the error on f is:

$$\frac{\sqrt{Npq}}{N} = \sqrt{pq/N} = \sqrt{f(1-f)/A} \quad (55)$$

## 5.1 centrality estimator

To estimate the centrality the V0 multiplicity is used for the regular points. However the centrality can also be estimated by using another detector such as CL1 or by using the TPC tracks. Here we compare what happens when we do that.

In the left panel of figure 28 the comparison between using different centrality estimators on  $v_2$  is shown. On the right hand of figure 28 the ratio with respect to the default measurement is shown. From this we estimate the systematic error coming from the centrality estimator which is listed in table 5. Since the systemics coming from different centrality estimators should be independent of  $p_T$ , the systematic error is kept reasonably small also for the higher  $p_T$  bins.

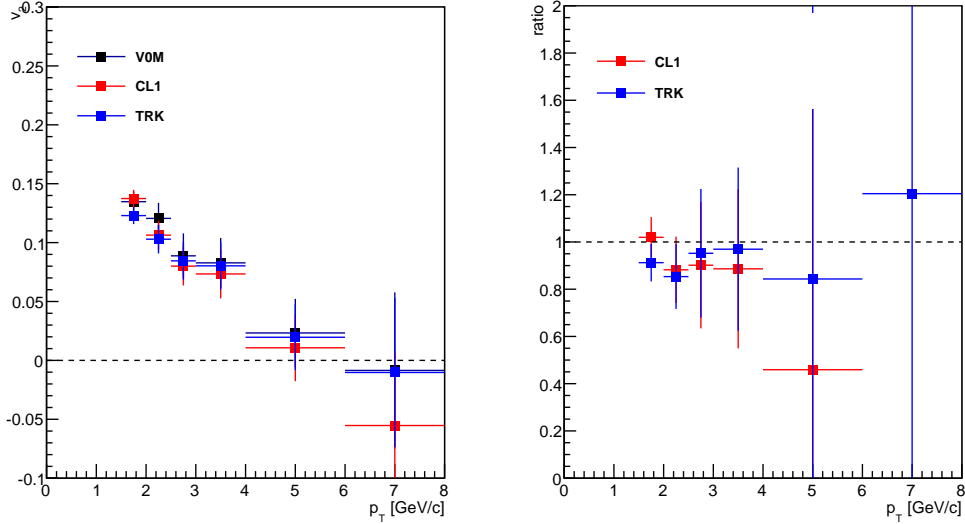


Figure 28: CL1 and TRK comparison

$p_T$	1.5-2	2-2.5	2.5-3	3-4	4-6	6-8
%	5	5	5	5	10	10

Table 5: centrality estimator

## 5.2 normalisation range

A comparison is made for changing the range of the  $E/p$  distribution which is used for normalising the hadron  $E/p$  distribution. The default points are normalised in the range  $0.2 < E/p < 0.7$ . The red points are normalised for points in the range  $0.2 < E/p < 0.4$ . On left side of figure 29 the difference in  $v_2$  is shown. On the right hand side of the same figure the ratio for the different normalisation range with the default measurement is made.

From the ratio plot the systematical contribution is taken as listed in table 6. For the highest  $p_T$  bin the systematical contribution was kept small as to not overestimate the statistical fluctuation.

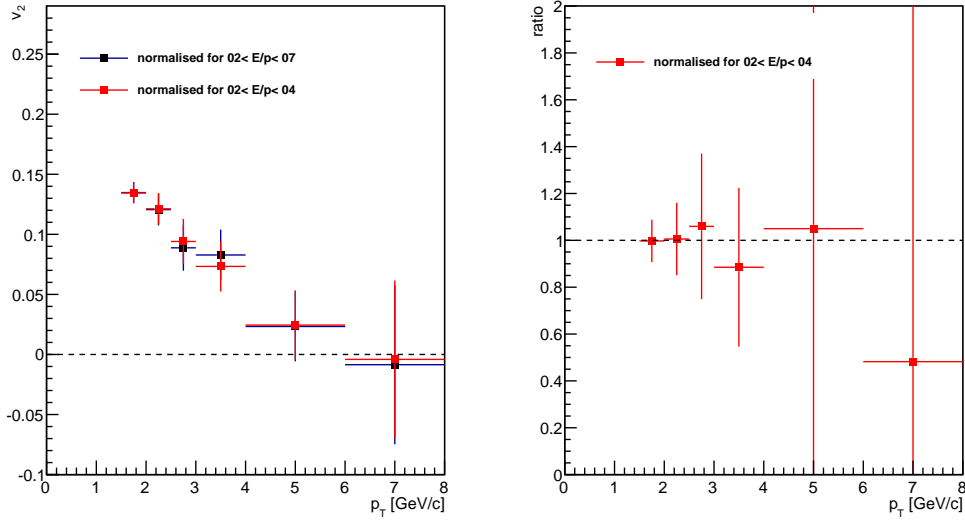


Figure 29: normalisation comparison

$p_T$	1.5-2	2-2.5	2.5-3	3-4	4-6	6-8
%	1	1	4	5	5	10

Table 6: normalisation range

### 5.3 binning

The effect of binning the E/p histogram before extracting the yield is checked. For the regular points we use a binning to make the fitting faster and easier. Here we compare these results with a run where we did not bin the results at all.

As for the centrality estimator binning the E/p histogram or not binning this histogram should be  $p_T$  independent. For this reason the systematic estimation is kept small in the highest  $p_T$  bin.

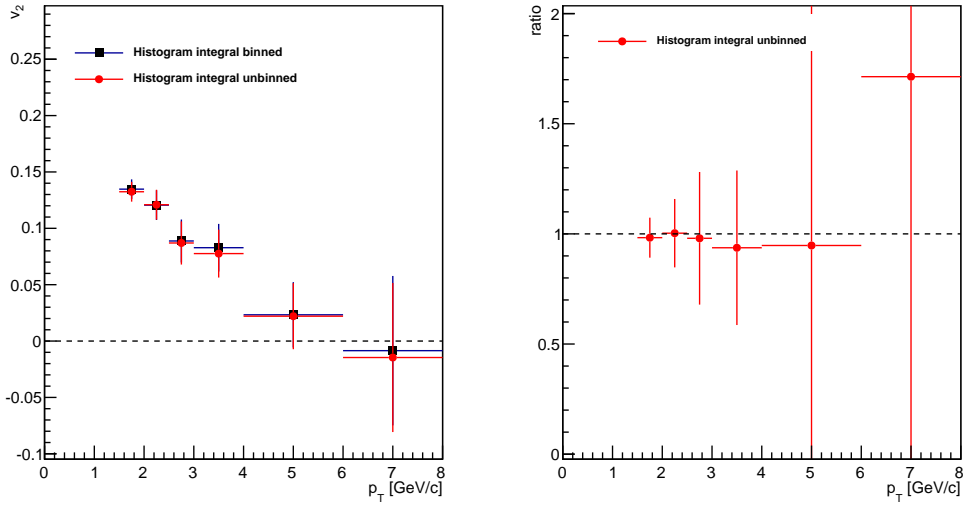


Figure 30: binning comparison

$p_T$	1.5-2	2-2.5	2.5-3	3-4	4-6	6-8
%	2	2	2	6	6	10

Table 7: binning



## 5.4 Yield extraction

As was already briefly mentioned in the previous chapter there are several methods for extracting the yield distribution. Here different yield extraction methods are explained for different background subtraction methods.

### 5.4.1 Fitting routine

After selecting the electrons using the cuts previously mentioned we plot the E/p distribution for 6 different  $p_T$  bins and 6 different  $\Delta\phi = \phi - \Psi$  bins. For each of these E/p distribution we fit the following function to the data;

$$f(x) = \frac{a}{b\sqrt{2\pi}} e^{-(x-c)^2/2b^2} + (\alpha + \beta x + \gamma x^2) \quad (56)$$

In figure 31<sup>9</sup> an example of such a fit on an E/p distribution is shown. In blue a gaussian plus second order polynomial is fitted. A gaussian with the same parameters is shown in green while the second order polynomial is plotted in red.

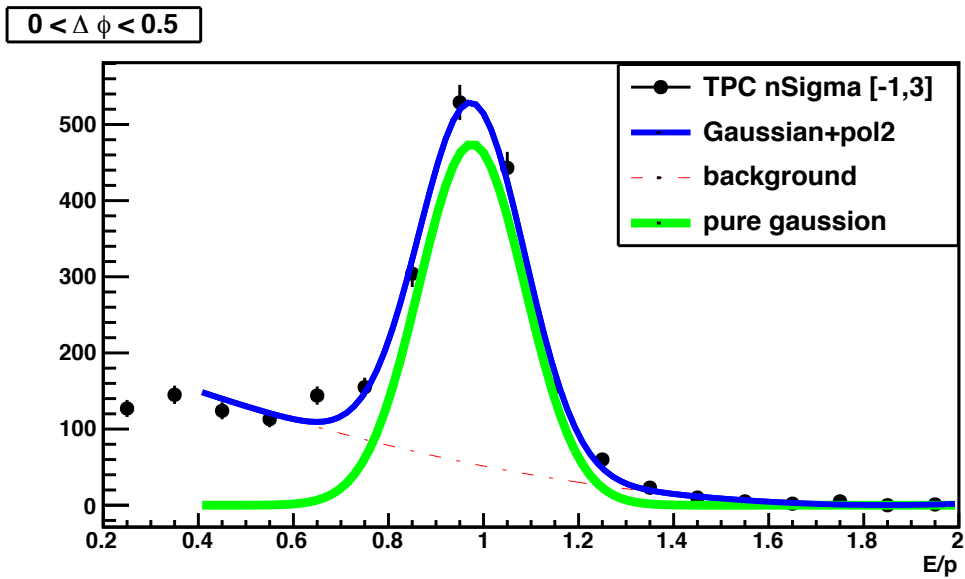


Figure 31: E/p distribution for  $1.5 < p_T < 2$ . Colours as in equation (56)

<sup>9</sup>Other bins can be found in the appendix

From these E/p distributions there are several ways to determine the raw yield. For each of the E/p distributions one point for the yield distribution can be calculated. This can be done by taking the fit parameter  $a$  or by integrating the fit function in one of the following ways;

$$\int_{c-3b}^{c+3b} \frac{a}{b\sqrt{2\pi}} e^{(x-c)^2/2b^2} + (\alpha + \beta x + \gamma x^2) dx - \int_{c-3b}^{c+3b} (\alpha + \beta x + \gamma x^2) dx \quad (57)$$

$$\int_{c-3b}^{c+3b} \frac{a}{b\sqrt{2\pi}} e^{(x-c)^2/2b^2} dx \quad (58)$$

The raw yield extracted in these three ways as well as the raw yield of the default measurement are plotted in figure 32<sup>10</sup> as a function of  $\Delta\phi$ .

The yield is then fitted with the following function;

$$\frac{dN}{d[\Delta\phi]} = N_0(1 + 2v_2^{obs} \cos(2\Delta\phi)) \quad (59)$$

Where  $N_0$  and  $v_2^{obs}$  are the unknown variables.

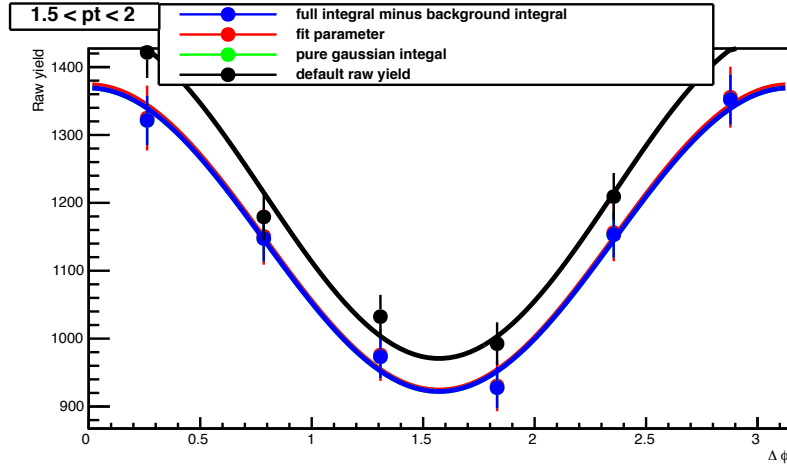


Figure 32: Raw Yield

<sup>10</sup>Other bins can be found in the appendix

The points calculated by using an integral over the pure gaussian (green) are in the same position as those for integrating the full function and subtracting the integral over the background function (blue).

For each  $p_T$  bin we extract  $v_2^{obs}$  from the fit.

This  $v_2^{obs}$  still has to be corrected for the resolution of the event plane resolution. In this case we correct  $v_2$  for the VZERO-A and the VZERO-C detector and combine the results in the following way;

$$v_2^{fin} = \frac{v_2^{V0A}/(\sigma v_2^{V0A})^2 + v_2^{V0C}/(\sigma v_2^{V0C})^2}{1/(\sigma v_2^{V0A})^2 + 1/(\sigma v_2^{V0C})^2} \quad (60)$$

Where the errors are propagated as;

$$\sigma v_2^{fin} = \sqrt{\frac{1}{1/(\sigma v_2^{V0A})^2 + 1/(\sigma v_2^{V0C})^2}} \quad (61)$$

We then get a final  $v_2$  as shown in figure 33.

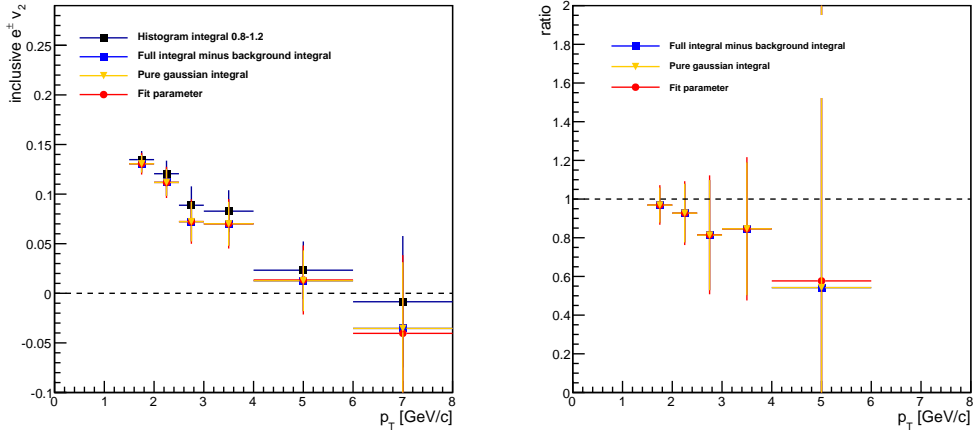


Figure 33: final  $v_2$

As for the raw yield all of the methods give a lower value than the default measurement. We also see that all of the yield extraction methods give nearly the same value for  $v_2$  as expected since the yield was the nearly same for all methods.

### 5.4.2 Data driven method

When using a data driven method a cut is applied on TPC  $N\sigma$  for electrons to be in the range  $[-1,3]$  and also a cut is made on the TPC  $N\sigma$  for hadrons  $[-10,-3.5]$ . The selected hadron tracks are then normalised in the lower range of the electron  $E/p$  distribution (in the  $E/p$  range from 0.2 to 0.7). This normalisation is necessary since the number of hadrons selected in the  $[-10,-3.5]$  range is much larger than the number of electrons selected in the  $[-1,3]$  of TPC  $N\sigma$  range.

In figure 34<sup>11</sup> the hadron  $E/p$  distribution after normalisation is shown (red) as well as the electron  $E/p$  distribution before subtracting the background (black).

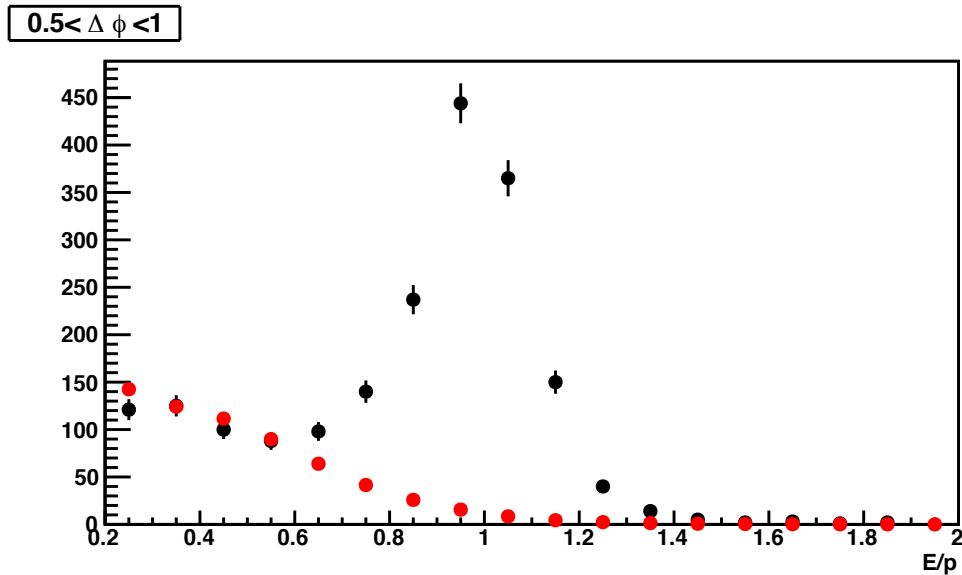


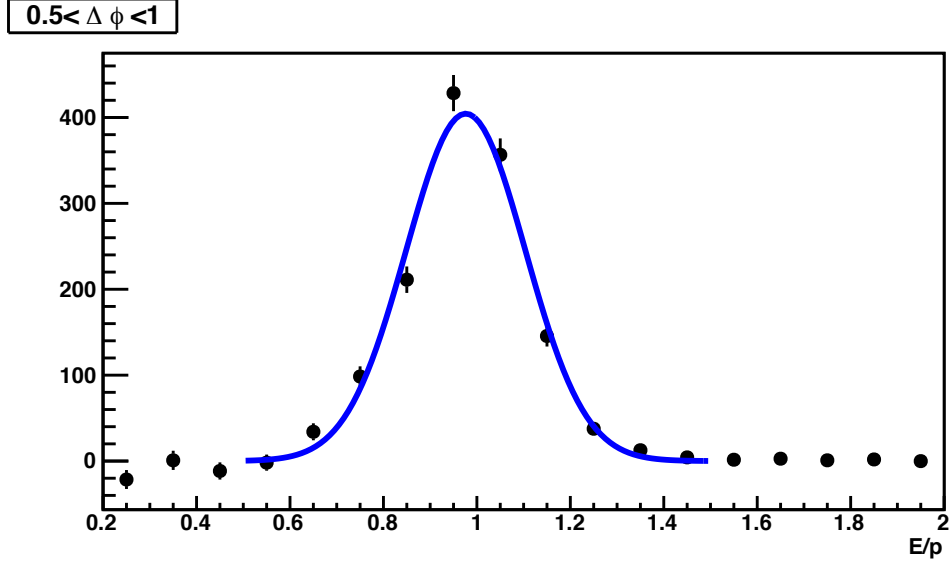
Figure 34:  $E/p$   $1.5 < p_T < 2$

After this renormalisation we subtract the hadron distribution from the electron distribution. To extract the signal we can fit a gaussian function.

$$f(x) = \frac{a}{b\sqrt{2\pi}} e^{-(x-c)^2/2b^2} \quad (62)$$

The  $E/p$  distribution after the subtraction of hadrons with this fit is shown in figure 35<sup>10</sup>.

<sup>11</sup>Other bins can be found in the appendix

Figure 35:  $E/p$   $1.5 < p_T < 2$ 

As before we have several possible ways of extracting the yield, though slightly different ones; integrating the fit function, taking the fit parameter  $a$  or integrating the histogram directly as was done for our default measurement (here indicated in green).

$$\int_{0.8}^{1.2} \frac{a}{b\sqrt{2\pi}} e^{(x-c)^2/2b^2} dx \quad (63)$$

$$\int_{c-3b}^{c+3b} \frac{a}{b\sqrt{2\pi}} e^{(x-c)^2/2b^2} dx \quad (64)$$

$$\int_{0.8}^{1.2} x_i dx \quad (65)$$

To these points we again fit the following function;

$$\frac{dN}{d[\Delta\phi]} = N_0(1 + 2v_2^{obs} \cos(2\Delta\phi)) \quad (66)$$

Where  $N_0$  and  $v_2^{obs}$  are the free parameters. All four options for extracting the yield and the fits are shown in figure 36<sup>12</sup>.

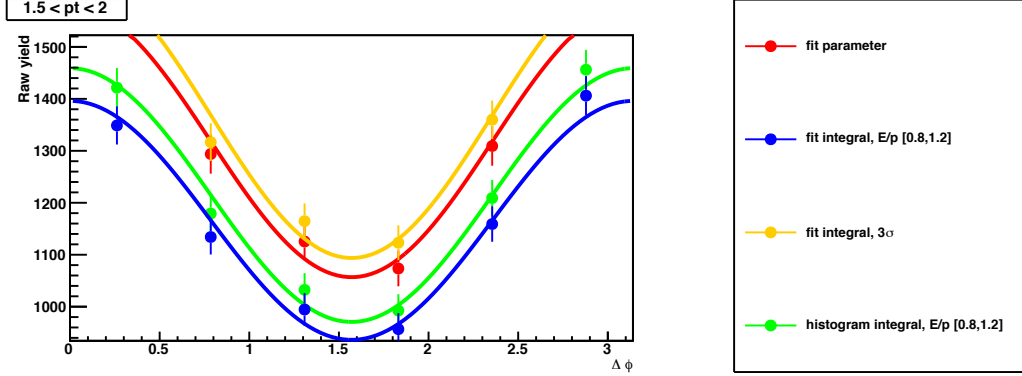


Figure 36: Raw Yield

This time you can see that the different methods do give different results. To minimise the errors we decided to use the direct integral of the histogram. Since this method does not require an extra step of fitting that could contribute to the error.

From the  $\frac{dN}{d[\Delta\phi]}$  fit we now extract  $v_2^{obs}$ .

The observed  $v_2$  is then corrected for the VZERO-A and the VZERO-C detector. The results from VZERO-A and VZERO-C are combined in the following way;

$$v_2^{fin} = \frac{v_2^{V0A}/(\sigma v_2^{V0A})^2 + v_2^{V0C}/(\sigma v_2^{V0C})^2}{1/(\sigma v_2^{V0A})^2 + 1/(\sigma v_2^{V0C})^2} \quad (67)$$

Where the errors are propagated as;

$$\sigma v_2^{fin} = \sqrt{\frac{1}{1/(\sigma v_2^{V0A})^2 + 1/(\sigma v_2^{V0C})^2}} \quad (68)$$

In figure 37 we see the results for the different yield extraction methods within the data driven method.

The combined systematic studies for different yield extraction methods are summarised in table 8.

<sup>12</sup>Other bins can be found in the appendix

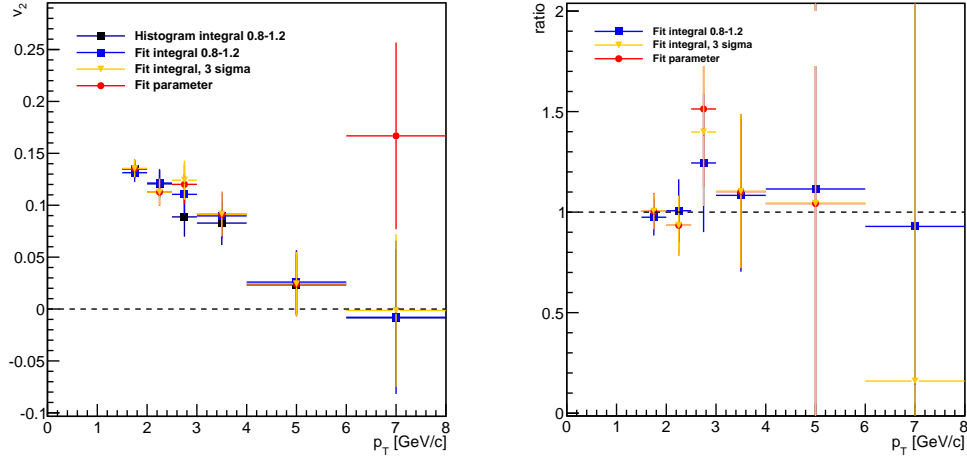


Figure 37: method comparison

We only include different methods used for yield extraction in the data driven method in the systematic studies since we have already seen that this method is a better way of removing hadron contamination than the fitting routine.

$p_T$	1.5-2	2-2.5	2.5-3	3-4	4-6	6-8
%	2	2	5	5	5	10

Table 8: yield extraction methods comparison

### 5.5 number of $\Delta\phi$ bins

The default measurement for  $v_2$  is determined by using six  $\phi - \Psi$  bins. The comparison is made with using ten  $\phi - \Psi$  bins.

The number of  $\Delta\phi$  bins used should not depend on the  $p_T$  which is why the systematic estimation is kept small at high  $p_T$ . We also see that for the lowest  $p_T$  bins the difference in the final  $v_2$  is very small.

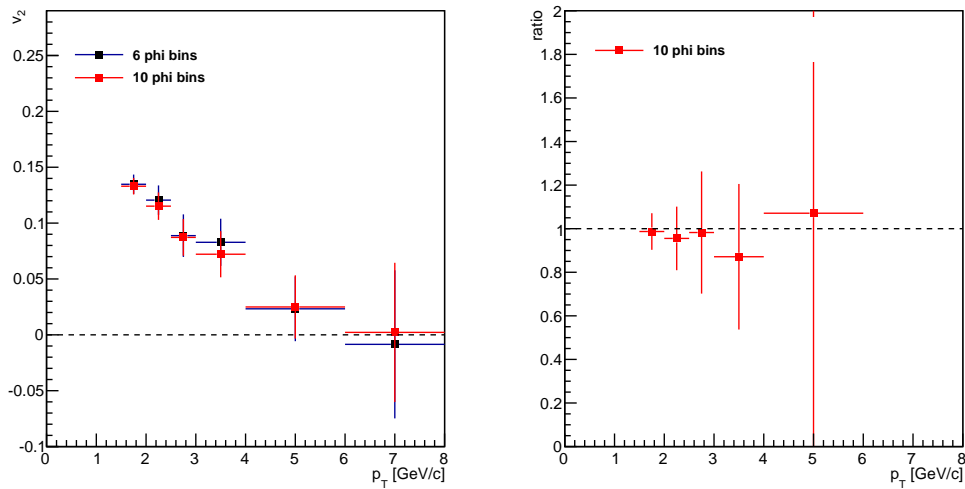


Figure 38: number of delta phi bins comparison

$p_T$	1.5-2	2-2.5	2.5-3	3-4	4-6	6-8
%	1	1	1	5	5	10

Table 9: number of delta phi bins



## 5.6 TPC $N\sigma$ range

We selected electrons in a TPC  $N\sigma$  range between  $[-1,3]$ . However the electrons could be selected by using slightly different cuts. Here a comparison is made for different ranges for selecting electron with TPC  $N\sigma$ . Two tighter cuts and one looser cut is tested. We see that for lower  $p_T$  bins the systematics are minimal while for higher  $p_T$  the systematics are higher.

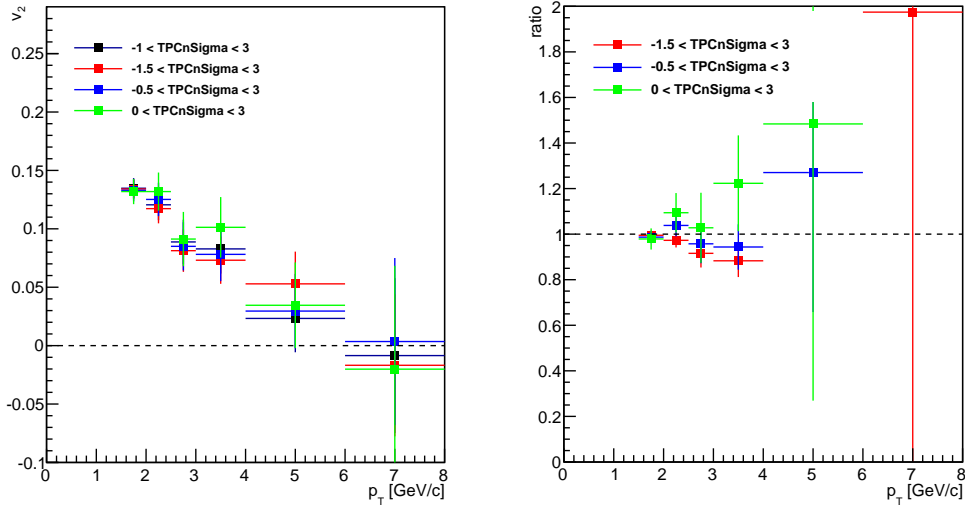


Figure 39: TPC  $n\sigma$  comparison

$p_T$	1.5-2	2-2.5	2.5-3	3-4	4-6	6-8
%	2	5	5	5	15	15

Table 10: TPC  $n\sigma$

## 5.7 E/p range

Here we compare our regular calculation of  $v_2$  with taking different E/p ranges for integrating the histogram. This is shown in figure 40. One smaller and one larger range is tested.

We see that for higher  $p_T$  bins the effect of the integration range is higher than for lower  $p_T$  bins.

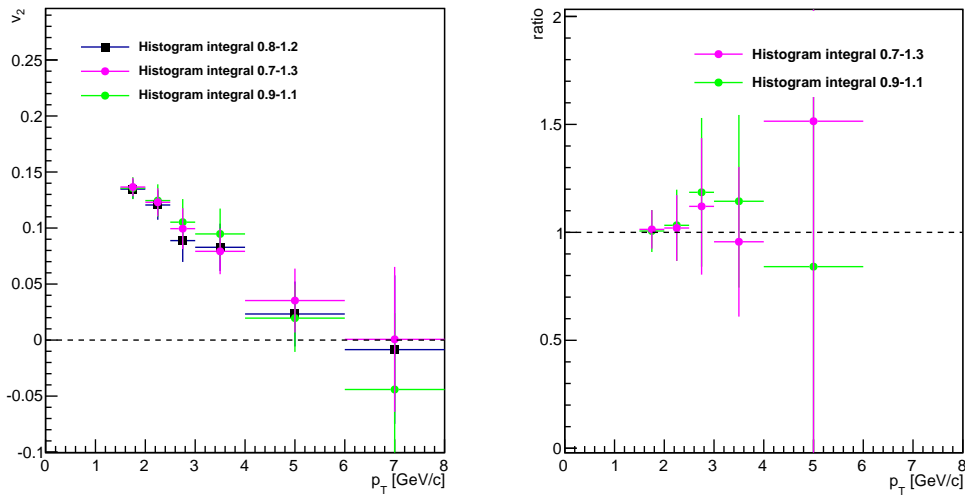


Figure 40: yield extraction comparison E/p range

$p_T$	1.5-2	2-2.5	2.5-3	3-4	4-6	6-8
%	5	5	5	5	15	15

Table 11: E/p range

## 5.8 shower shape cut

Last we compare the results with the shower shape cut, without this cut and with a different shower shape cut. In figure 41 the effect for the three different shower shape cuts explained in section 4.3 on the final  $v_2$  is shown and a summary of the systematics is stated in table 12.

As expected there are substantial differences observed in  $v_2$  when using a different or no shower shape cut.

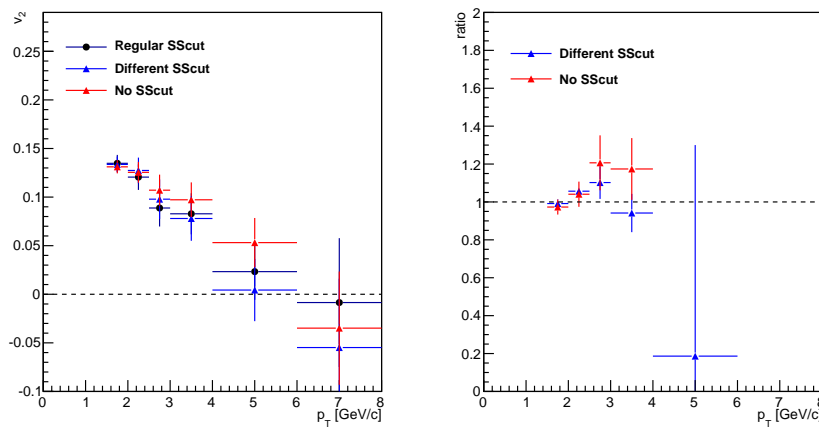


Figure 41: SS cuts comparison

$p_T$	1.5-2	2-2.5	2.5-3	3-4	4-6	6-8
%	2	3	10	10	15	15

Table 12: SS cuts

## 5.9 systematics summary

In figure 42 the systematics coming from all the systematic studies for particle identification are shown. Since changing particle identification cuts effect the purity of the electron sample we expect the final elliptic flow to differ for these studies which is reflected in these plots.

The systematics coming from these systematic studies are summarised in table 13.

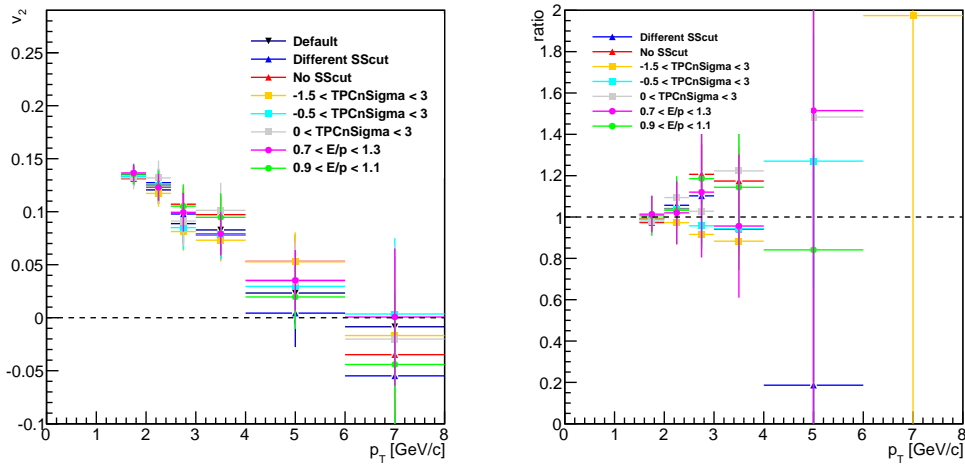


Figure 42: systematics for particle identification studies

$p_T$	1.5-2	2-2.5	2.5-3	3-4	4-6	6-8
TPC $n\sigma$ [%]	2	5	5	5	15	15
E/p range [%]	5	5	5	5	15	15
shower shape cuts [%]	2	3	10	10	15	15

Table 13: systematics for particle identification studies

Figure 43 shows the systematics for using a different binning for  $\Delta\phi$  and for binning the E/p distribution histogram. This figure also includes the systematics coming from the E/p range used for normalisation.

In table 14 the systematics coming from all non particle identification studies are summarised. This table includes the same studies as the figure and also includes the studies to the centrality estimator and the yield extraction method.

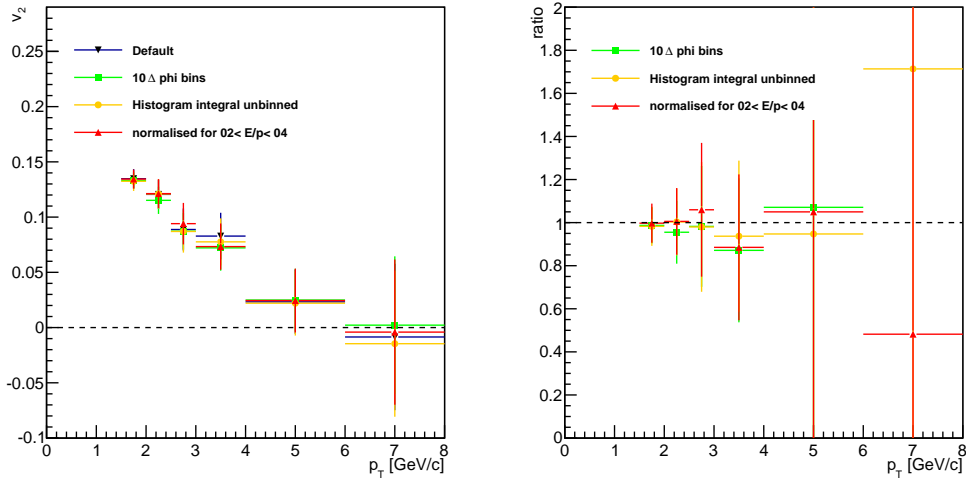


Figure 43: systematics of non particle identification studies

$p_T$	1.5-2	2-2.5	2.5-3	3-4	4-6	6-8
centrality estimator [%]	5	5	5	5	10	10
normalisation E/p range [%]	1	1	4	5	5	10
histogram binning [%]	2	2	2	6	6	10
# $\Delta\phi$ bins [%]	1	1	1	5	5	10
yield extraction method [%]	2	2	5	5	5	10

Table 14: systematics of non particle identification studies

## 6 Conclusions, discussions and outlook

All of the systematic studies conducted in the previous chapter are shown in the right hand side of figure 44. On the left hand side of the same figure the systematics are combined and shown as boxes around the final  $v_2$  points. To get the combined systematics the systematics of all previously explained studies were propagated quadratically.

Tables 15 and 16 summarise the combined systematic. In the same tables the statistical errors are shown.

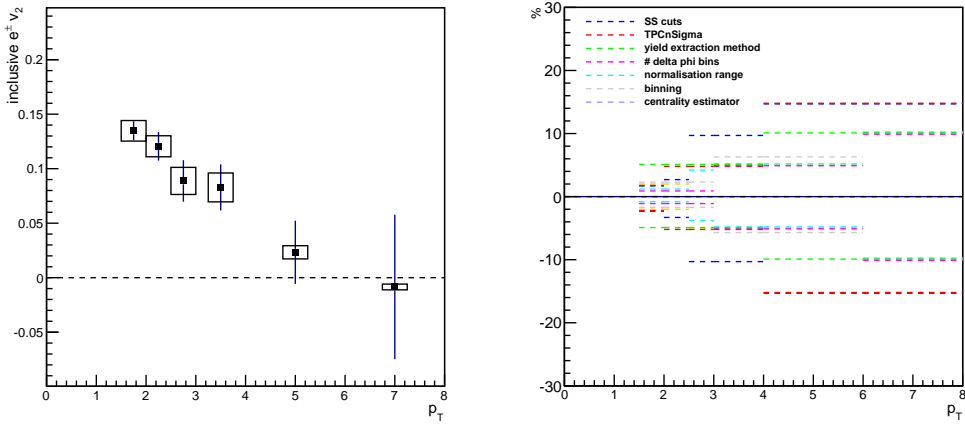


Figure 44: combined systematics

	1.5-2	2-2.5	2.5-3	3-4	4-6	6-8	$p_T$
systematics	7	8	14	16	26	31	%
statistics	6	11	21	25	125	774	%

Table 15: combined systematics

$p_T$	1.5-2	2-2.5	2.5-3	3-4	4-6	6-8
systematics	0.009	0.010	0.012	0.013	0.006	0.003
statistics	0.009	0.013	0.019	0.021	0.029	0.066

Table 16: absolute error

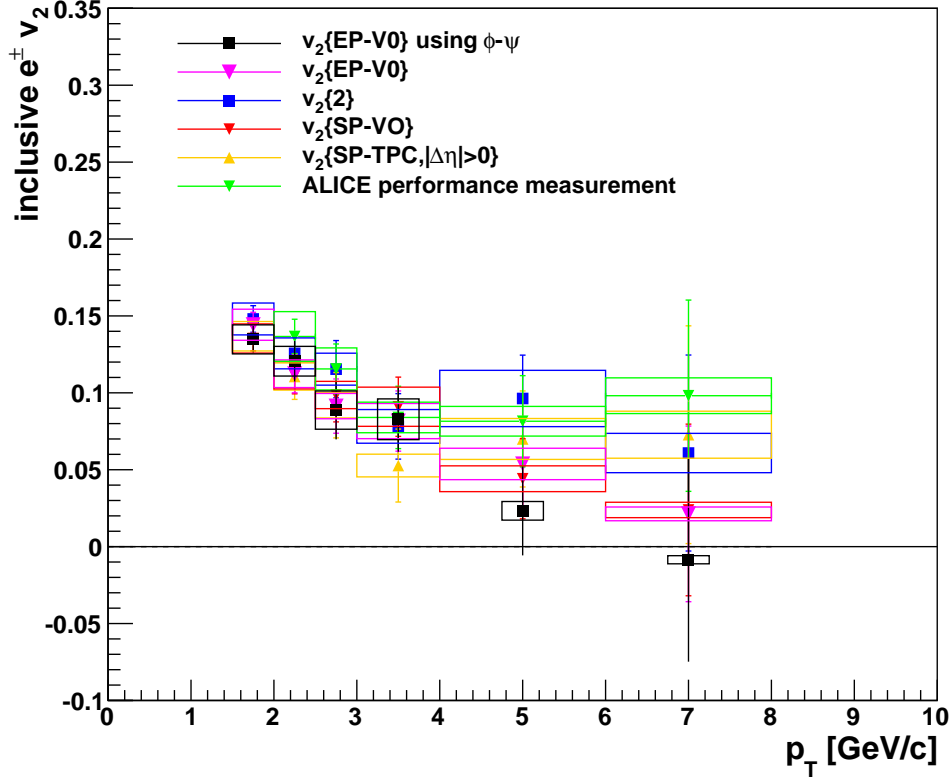


Figure 45: conclusion

We see that different methods are comparable within the error bars and systematics boxes. The  $\phi - \Psi$  method was implemented to check the effect of hadron contamination in the other methods. This method can work as a check since within the  $\psi - \Psi$  method the contamination can be subtracted at the yield level. The fact that all methods are comparable implies that effect of the contamination is not visible in the other methods.

We see that the methods are less comparable in the two highest  $p_T$  bins ( $4 < p_T < 6$  and  $6 < p_T < 8$ ). This can be explained by the limited statistics available at the time this study was conducted. This effect is reflected in the large error bars.

**Outlook** Eventually we want to study not only the inclusive electrons, but heavy flavour electrons as well. These electrons are created in the first stages of the collision and therefore carry information about the full collision history. To get the heavy flavour decay electron elliptic flow the evaluation of the background sources of  $v_2$  need to be studied. The different contributions to the background are;

- Photon conversion in the material.
- Dalitz decay of neutral mesons.
- Dielectron decay of light vector mesons.
- Quarkonia decay.

When we have analysed the possible background sources we can determine the flow of the total background in the following way:

$$v_2^{back} = \sum_i R_i v_2^i \quad (69)$$

where  $v_2^i$  are the elliptic flow of the different background sources and  $R_i$  are the weights applied since not all of the background sources contribute equally.

**1 Cocktail method** For the cocktail method the background is calculated in a simulation using measured hadrons as input.

**2 Invariant mass method** For the invariant mass method electron pairs from the decay of neutral mesons and gamma conversion are reconstructed. After that a correcting is applied to the yield for the efficiency of the reconstruction.

Heavy flavour electron elliptic flow ( $v_2^{HFe}$ ) is then obtained by subtracting the background from the inclusive electron in the following way:

$$v_2^{HFe} = \frac{(1 + R_{SB})v_2^{Incl} - v_2^{back}}{R_{SB}} \quad (70)$$

where

$$R_{SB} + 1 = N^{Incl} / N^{Allnon-HFe} \quad (71)$$

with

$$N^{Incl} = N^{HFe} + N^{Allnon-HFe} \quad (72)$$

and

$$N^{Allnon-HFe} = N^{ULS} - N^{LS} + (1/eff - 1)(N^{ULS} - N^{LS}) \quad (73)$$

where  $N^{ULS}$  are the number of opposite sign pairs,  $N^{LS}$  are the number of like-sign pairs and where the efficiency  $eff$  is computed using a monte carlo study.



## Appendix

When we use the fitting method for subtracting the background we get the following plots.

$$f(x) = \frac{a}{b\sqrt{2\pi}} e^{-(x-c)^2/2b^2} + (\alpha + \beta x + \gamma x^2) \quad (74)$$

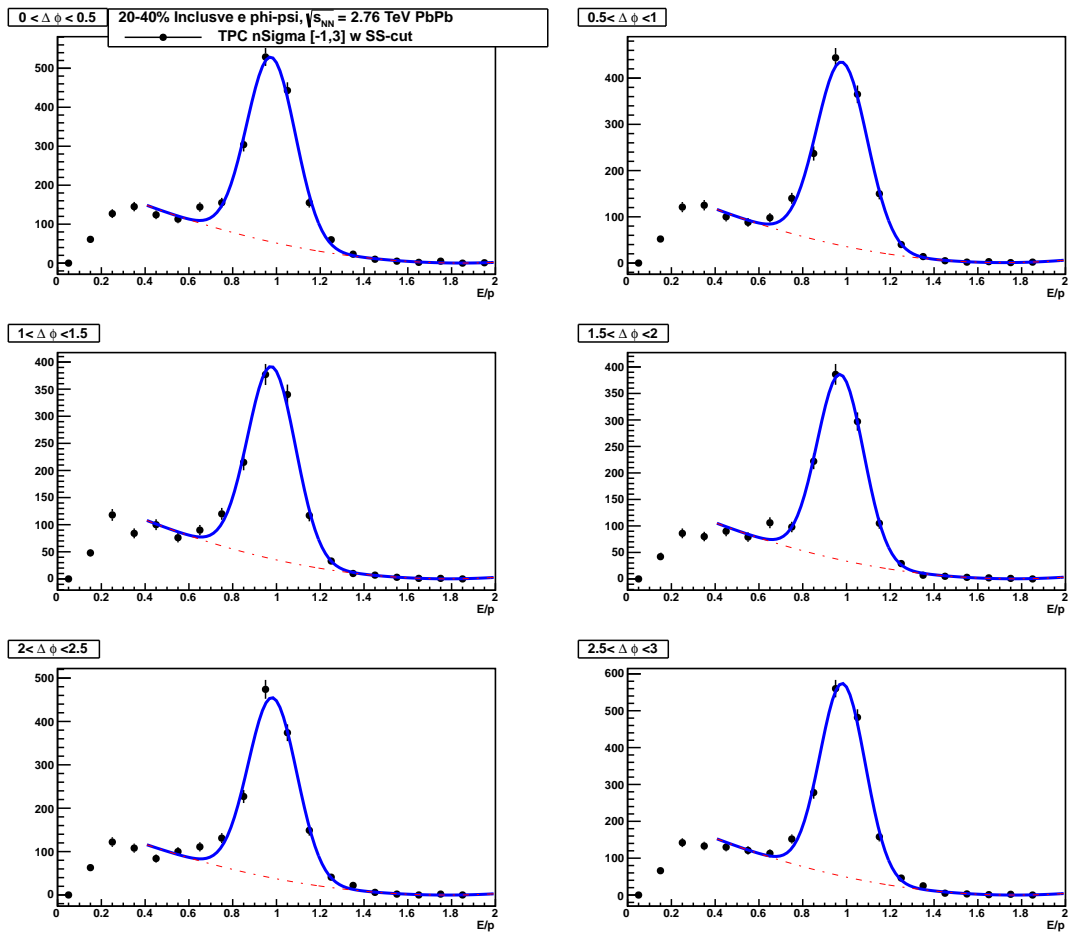


Figure 46:  $E/p$   $1.5 < p_T < 2$

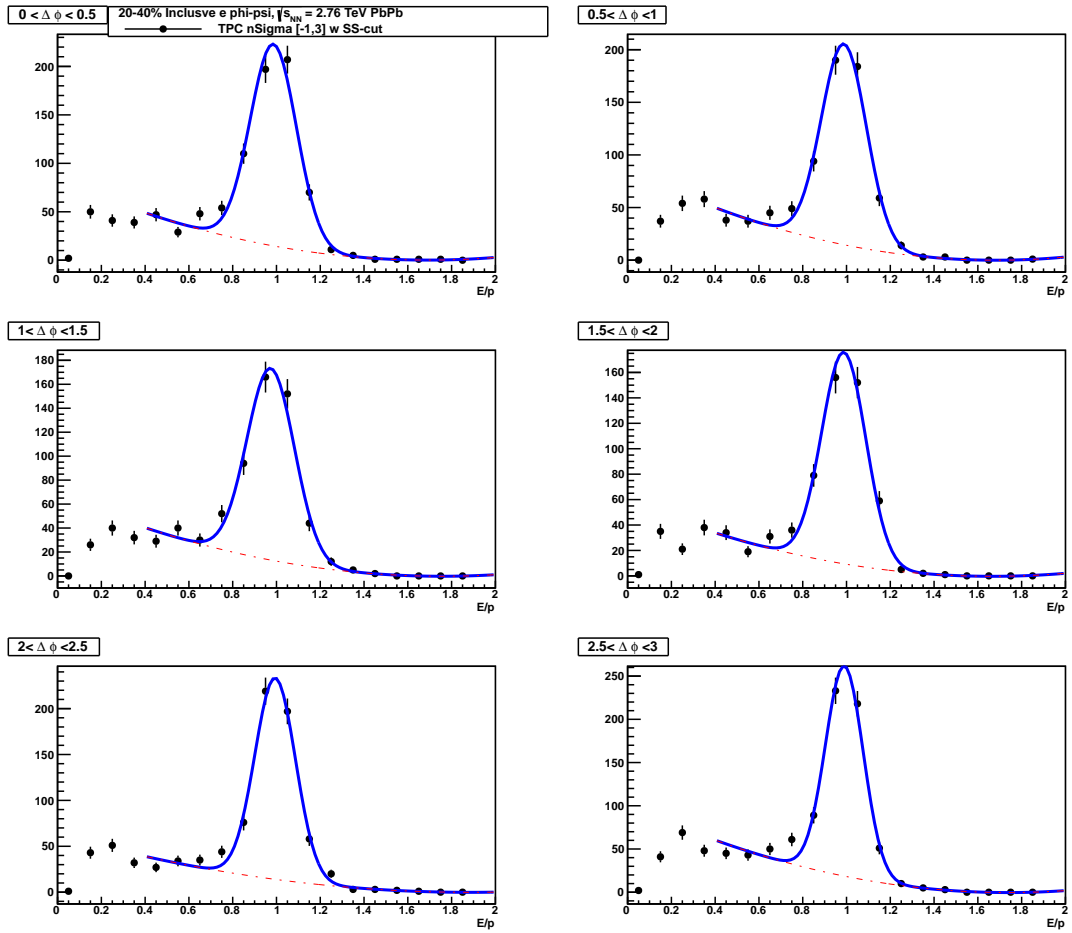


Figure 47:  $E/p$   $2 < p_T < 2.5$

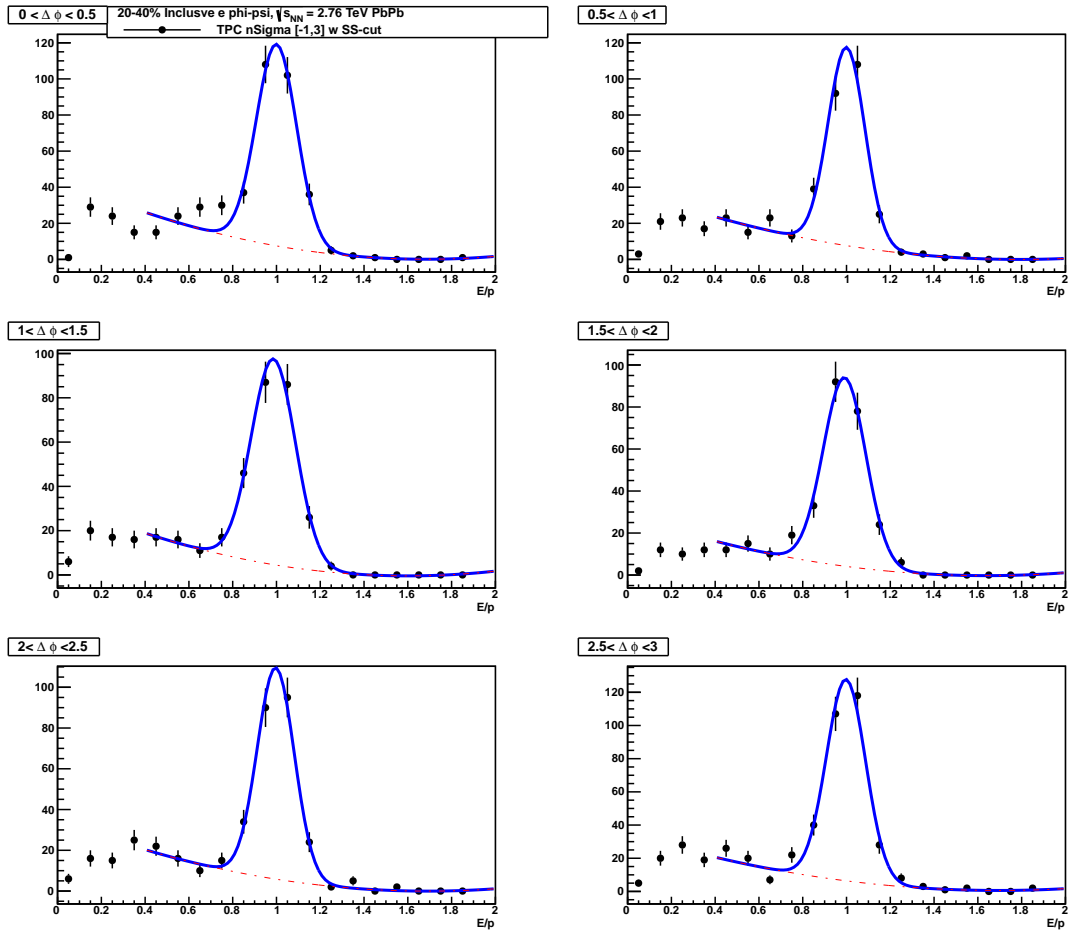


Figure 48:  $E/p$   $2.5 < p_T < 3$

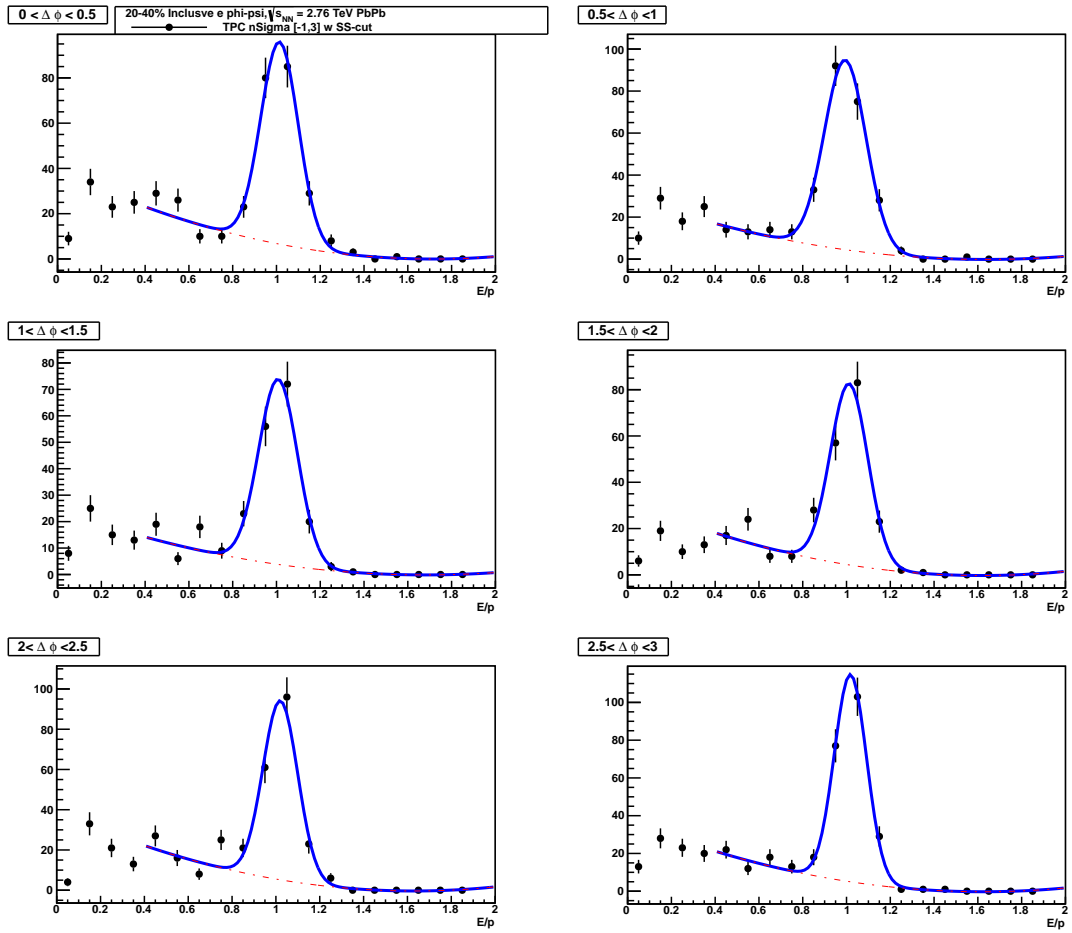


Figure 49:  $E/p$   $3 < p_T < 4$

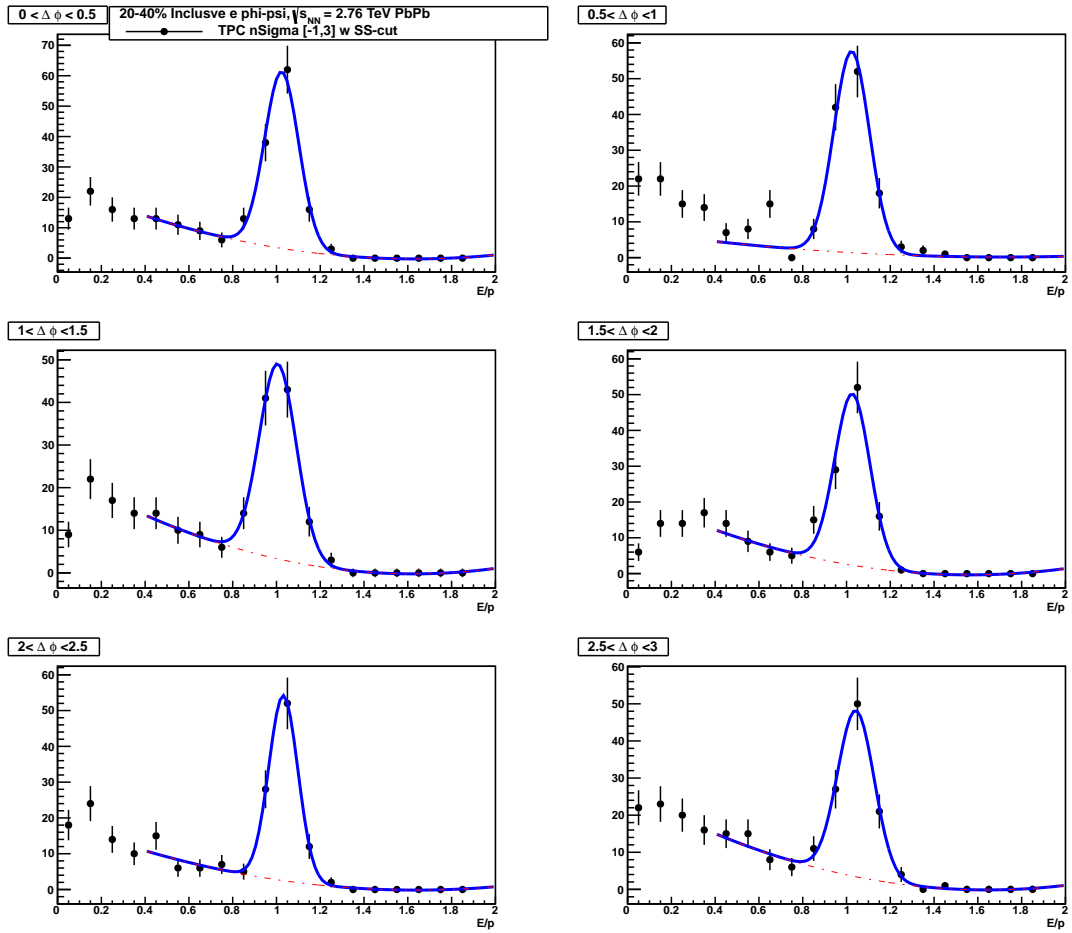


Figure 50:  $E/p$   $4 < p_T < 6$

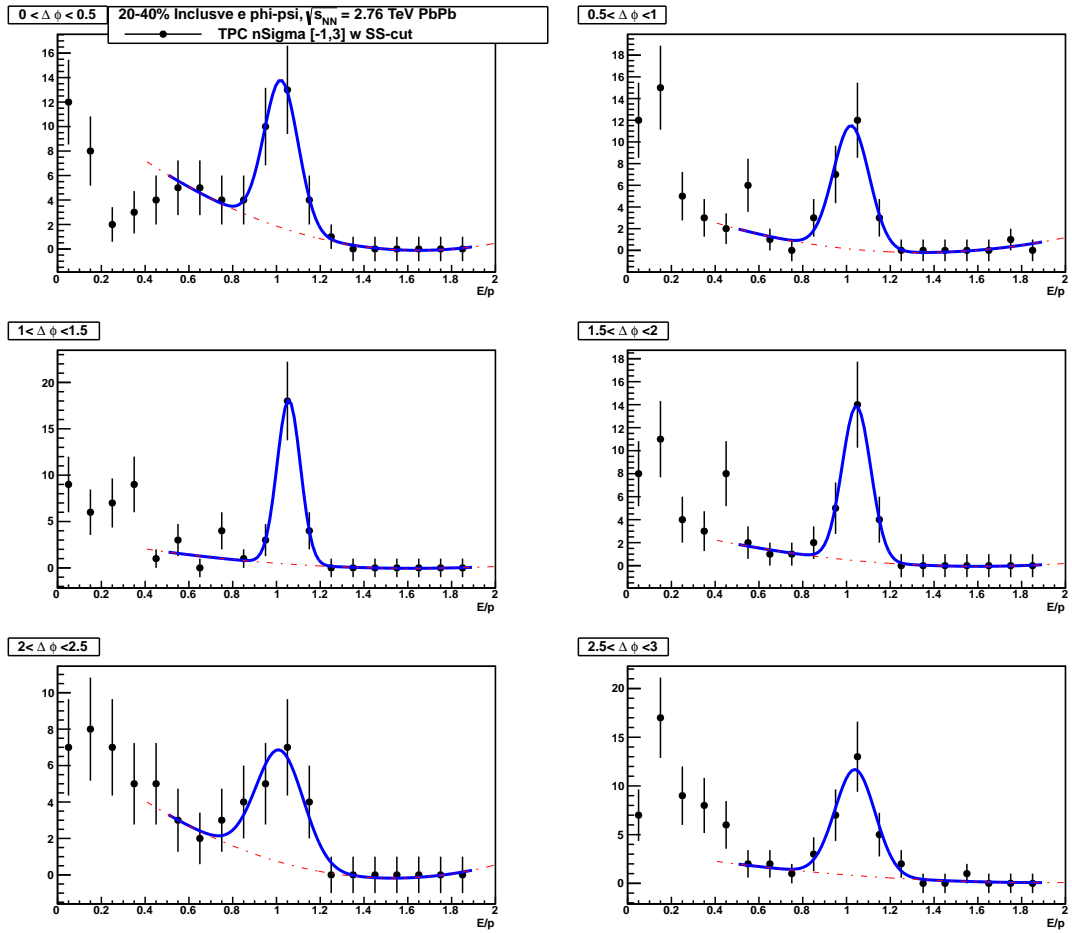


Figure 51:  $E/p$   $6 < p_T < 8$

When we use the data driven method we get the following plots for the renormalised background. The other  $p_T$  bins can be found when the background reduction is compared for the fitting method and the data driven method.

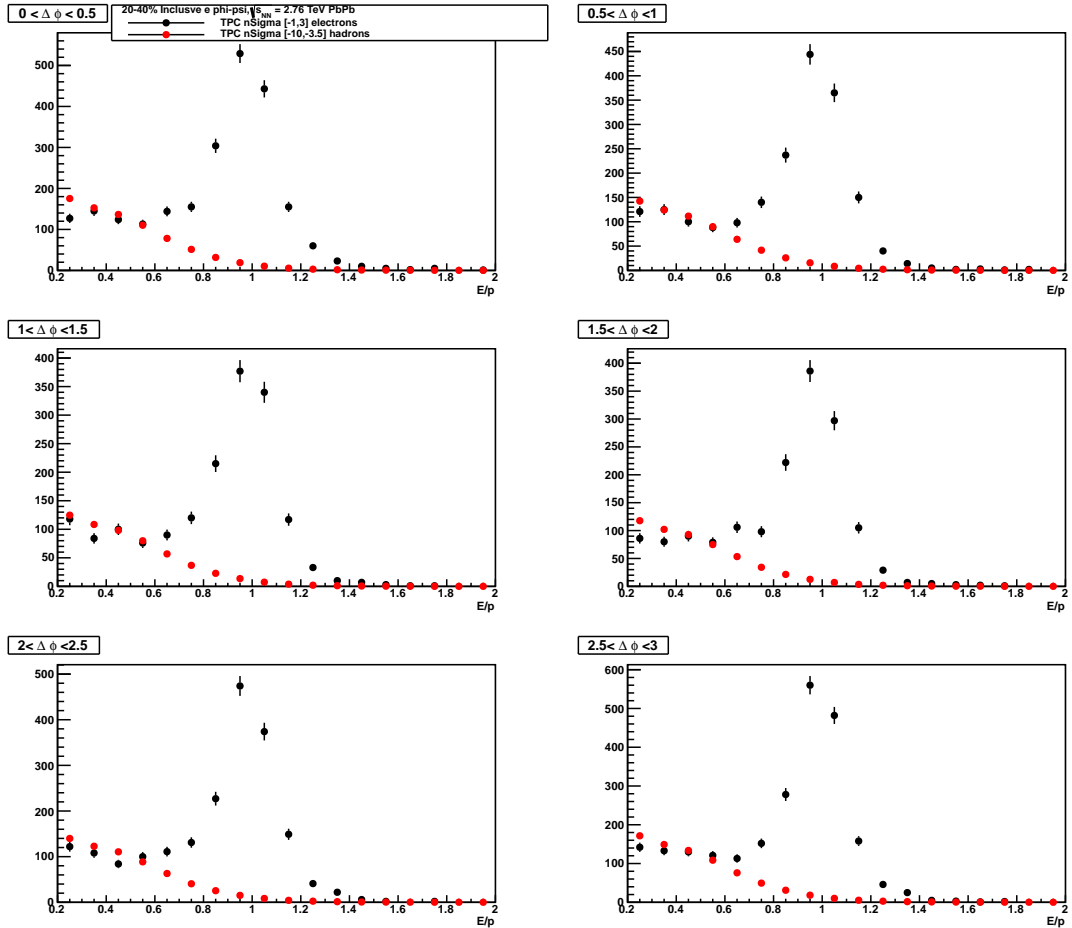


Figure 52:  $E/p$   $1.5 < p_T < 2$

When we fit a gaussian function after subtracting the background we get the following plots.

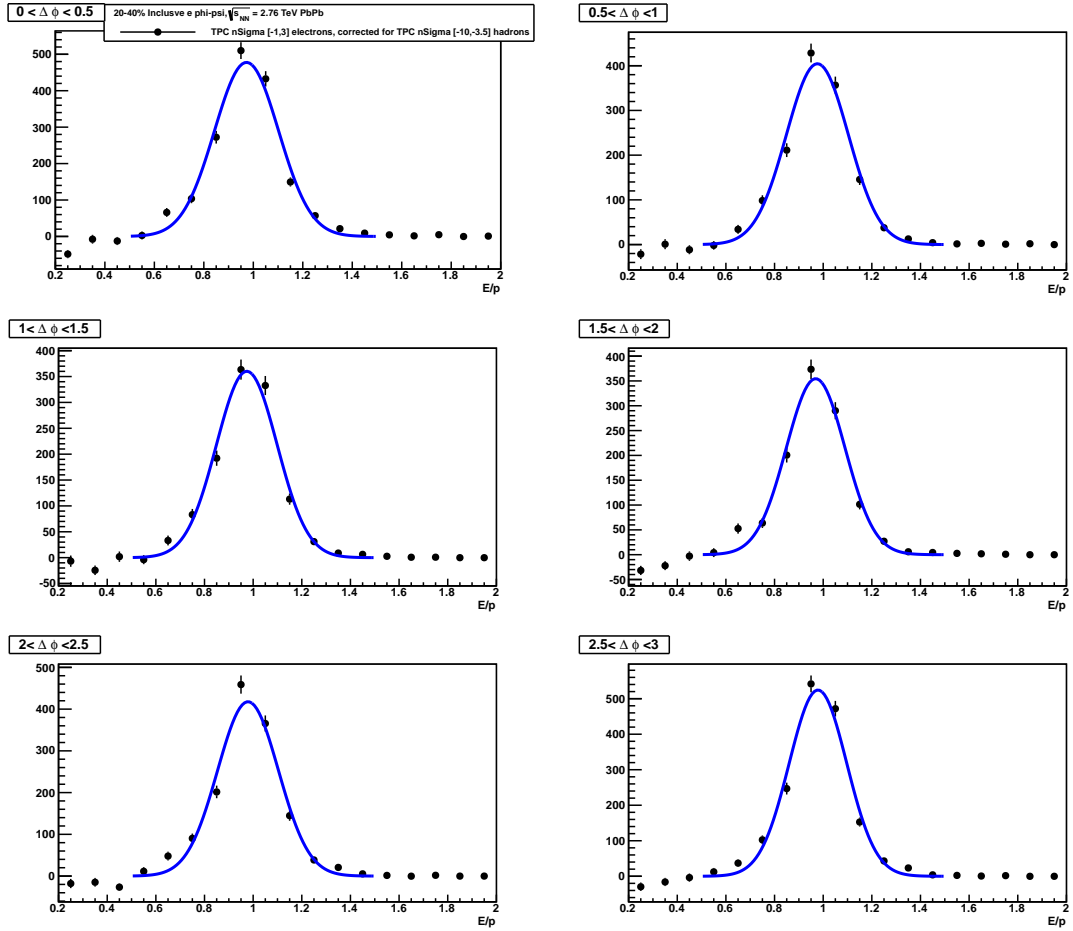


Figure 53:  $E/p$   $1.5 < p_T < 2$



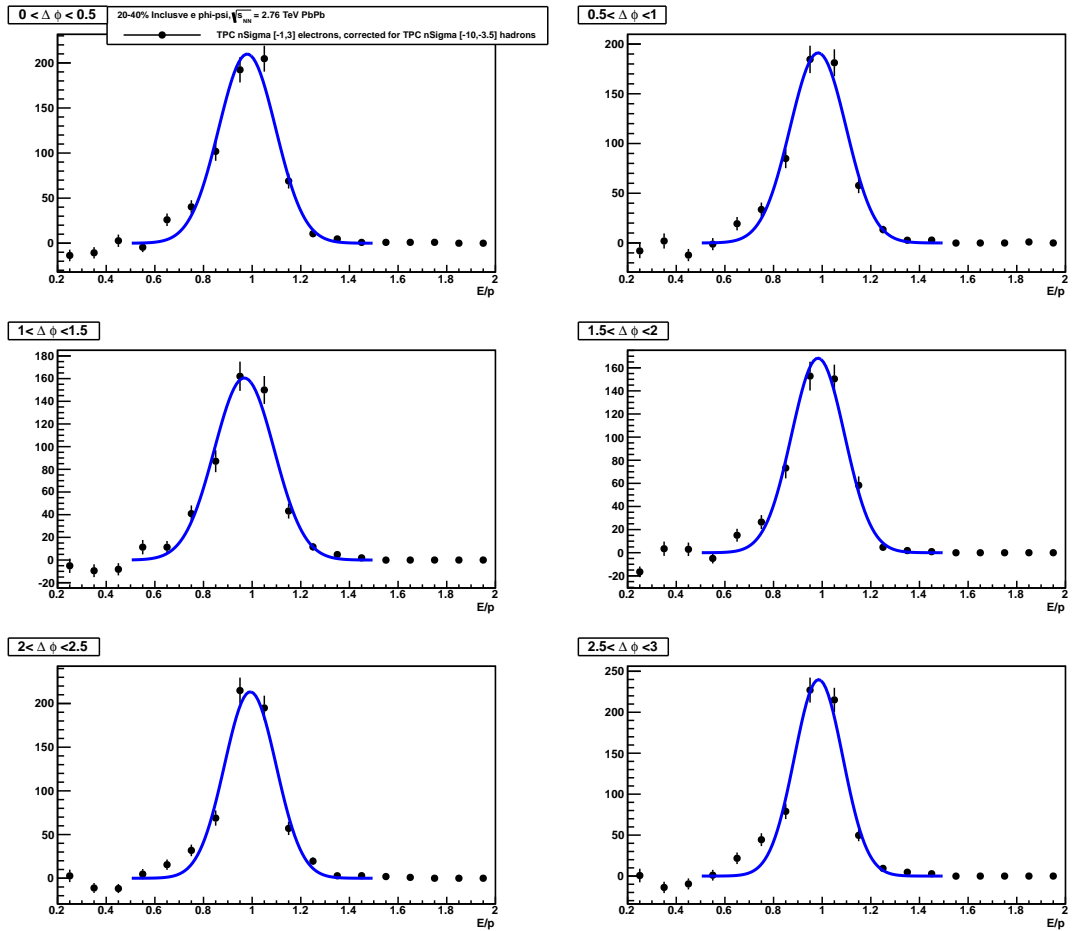


Figure 54:  $E/p$   $2 < p_T < 2.5$

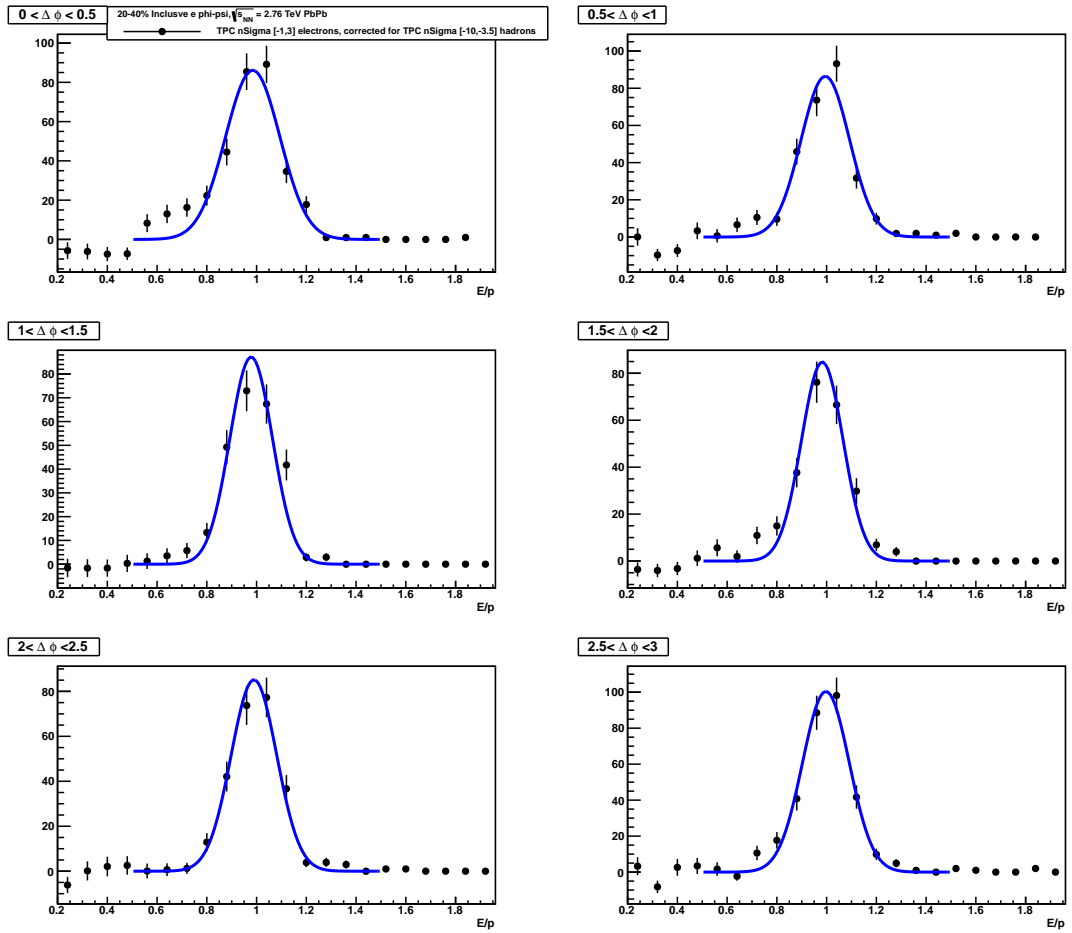


Figure 55:  $E/p$   $2.5 < p_T < 3$

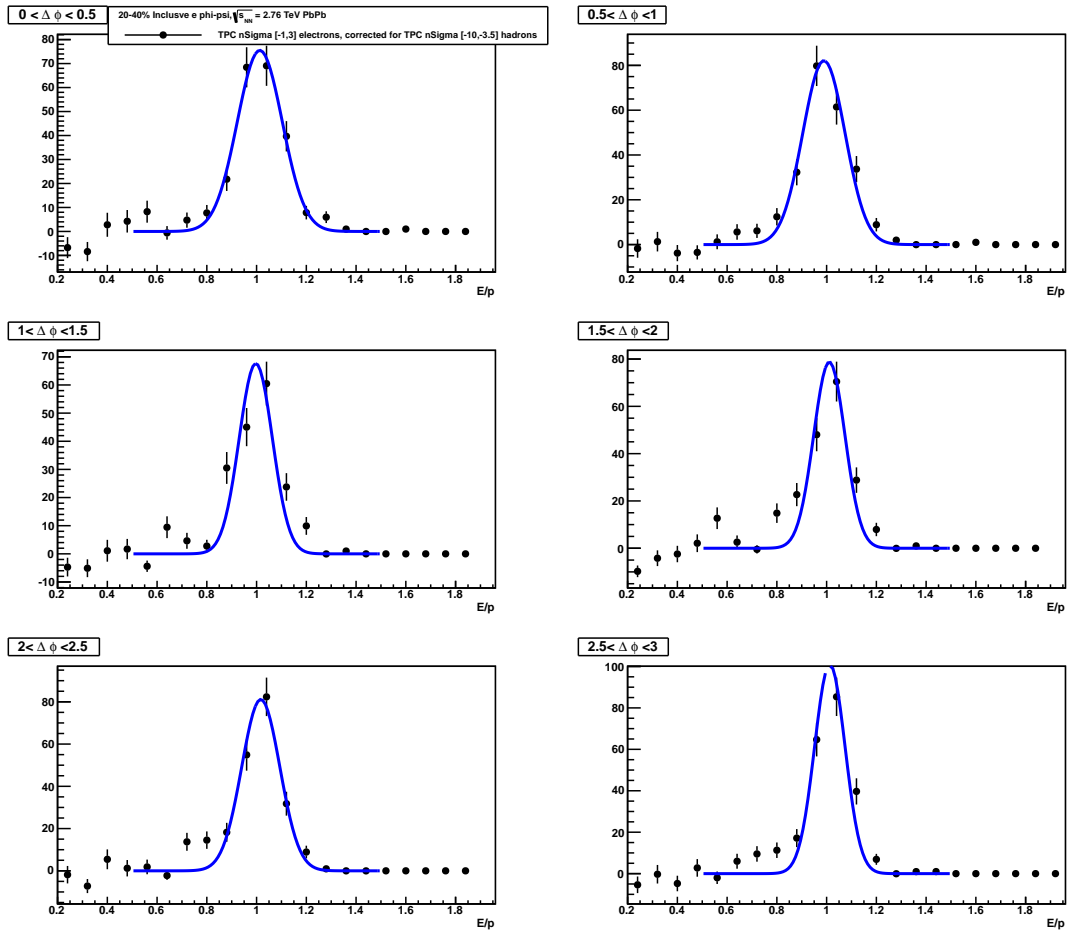


Figure 56:  $E/p$   $3 < p_T < 4$

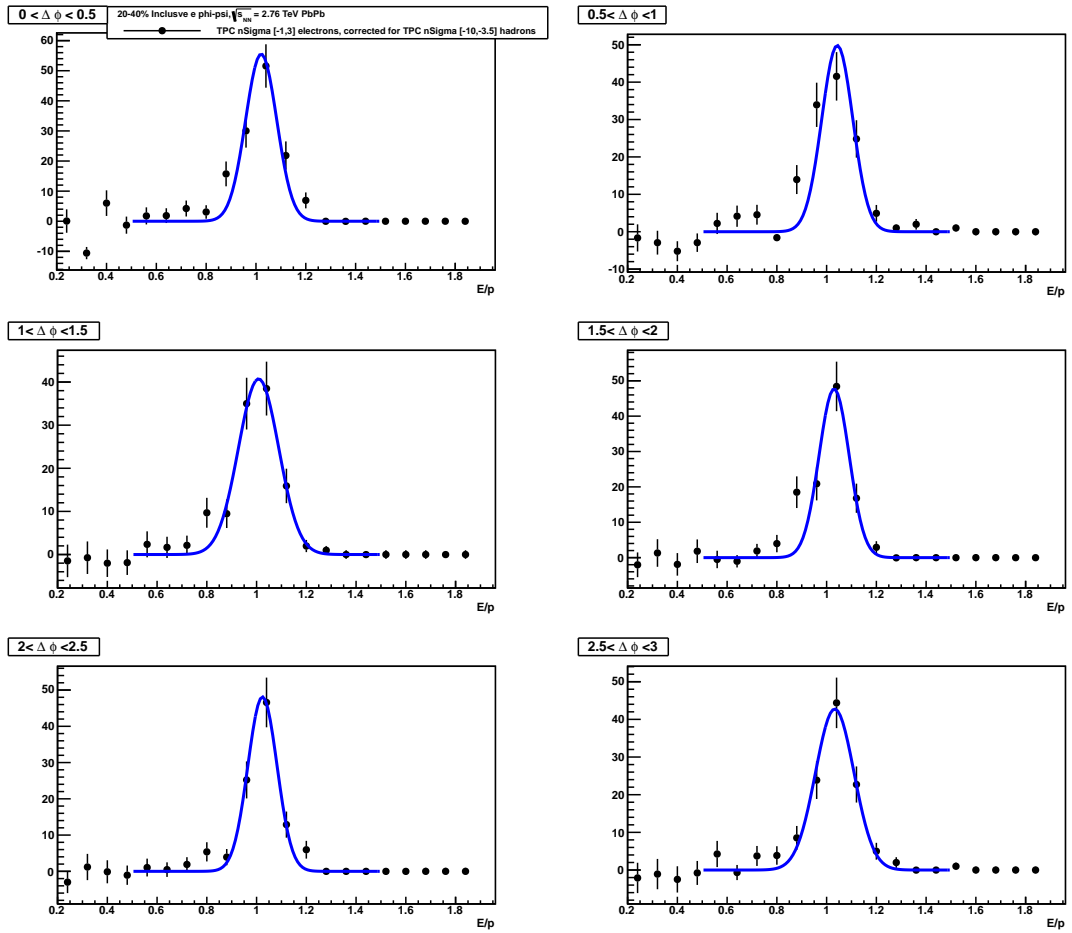


Figure 57:  $E/p$   $4 < p_T < 6$

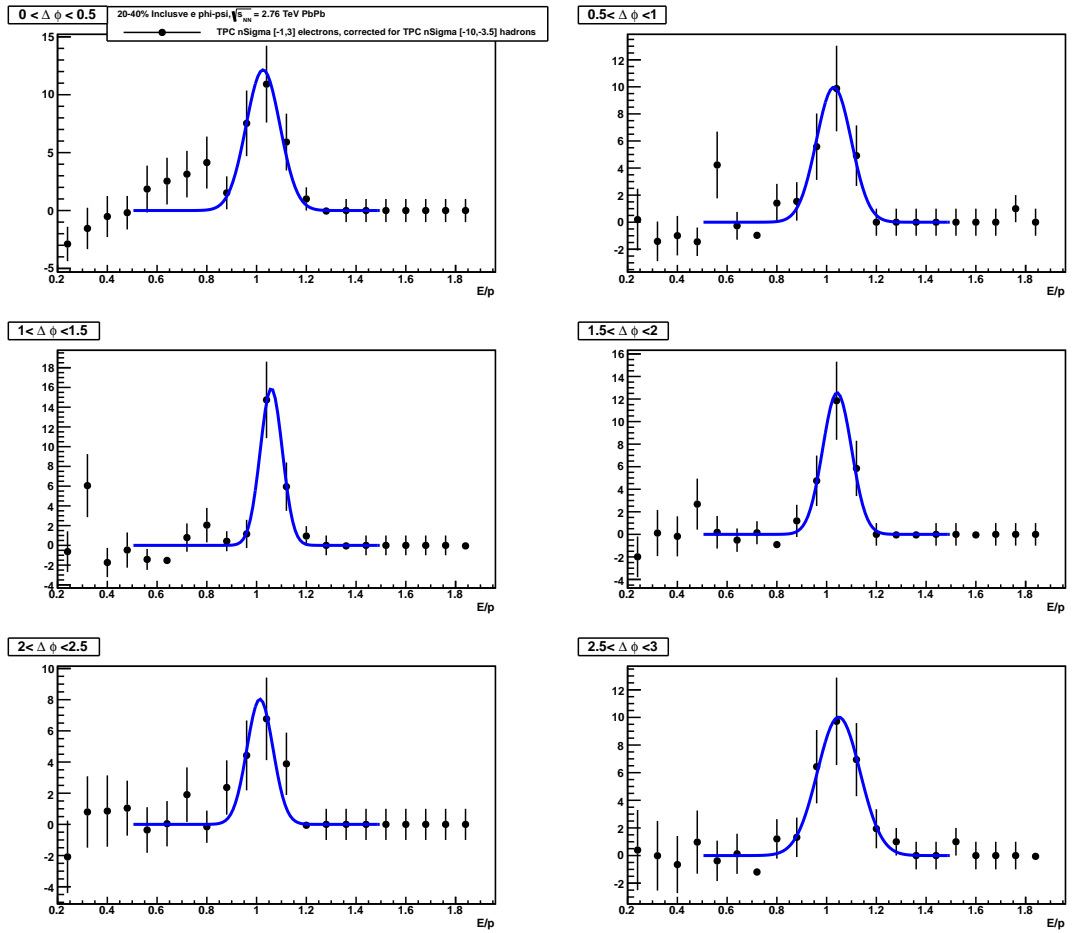


Figure 58:  $E/p$   $6 < p_T < 8$

For the yield we now get the following plots.

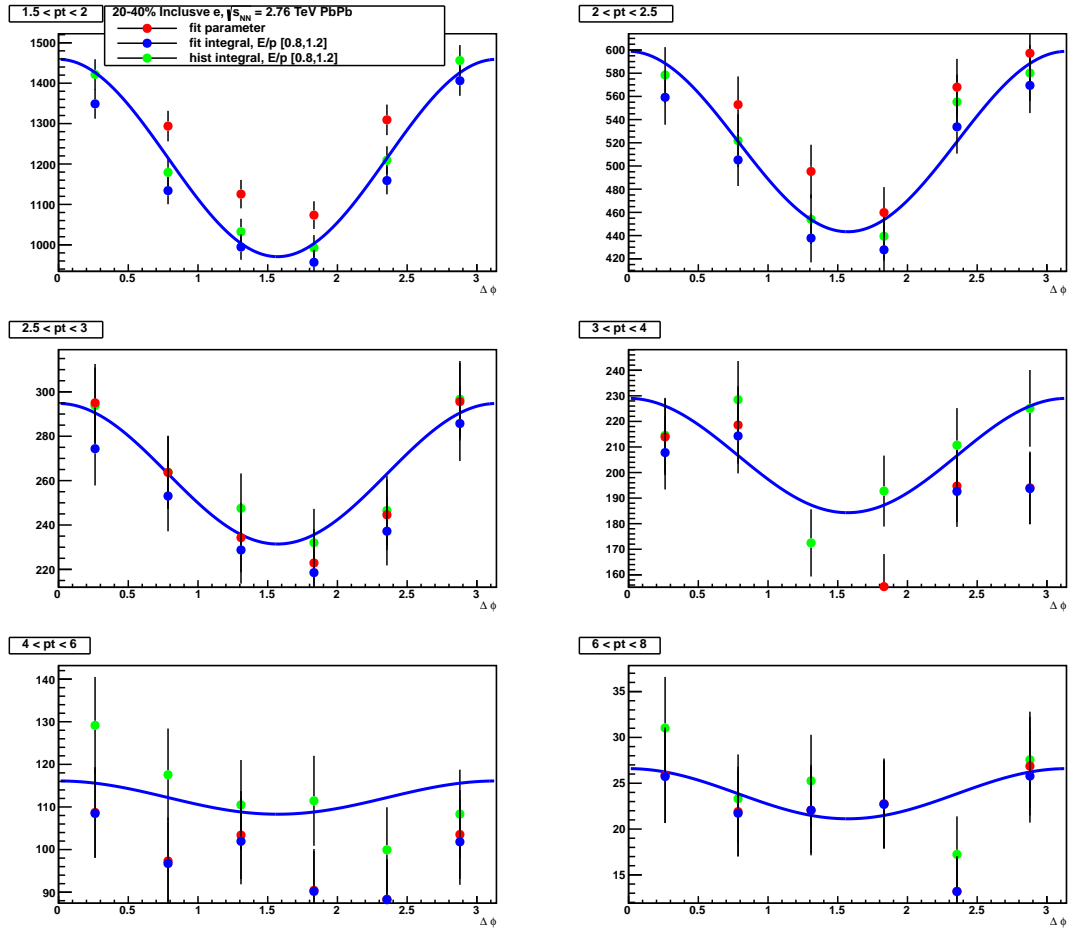


Figure 59: Raw Yield

Finally we compare the background reduction for the fitting method and the data driven method.

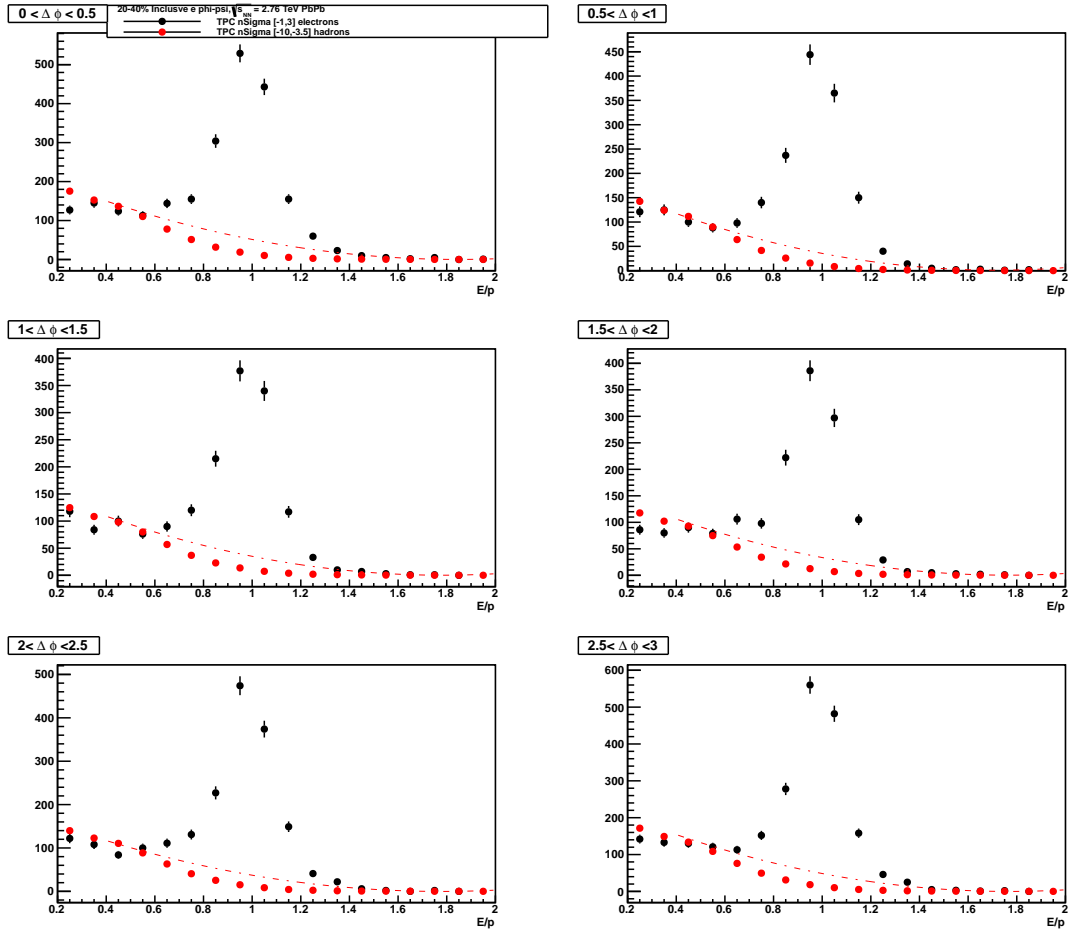


Figure 60:  $E/p$   $1.5 < p_T < 2$

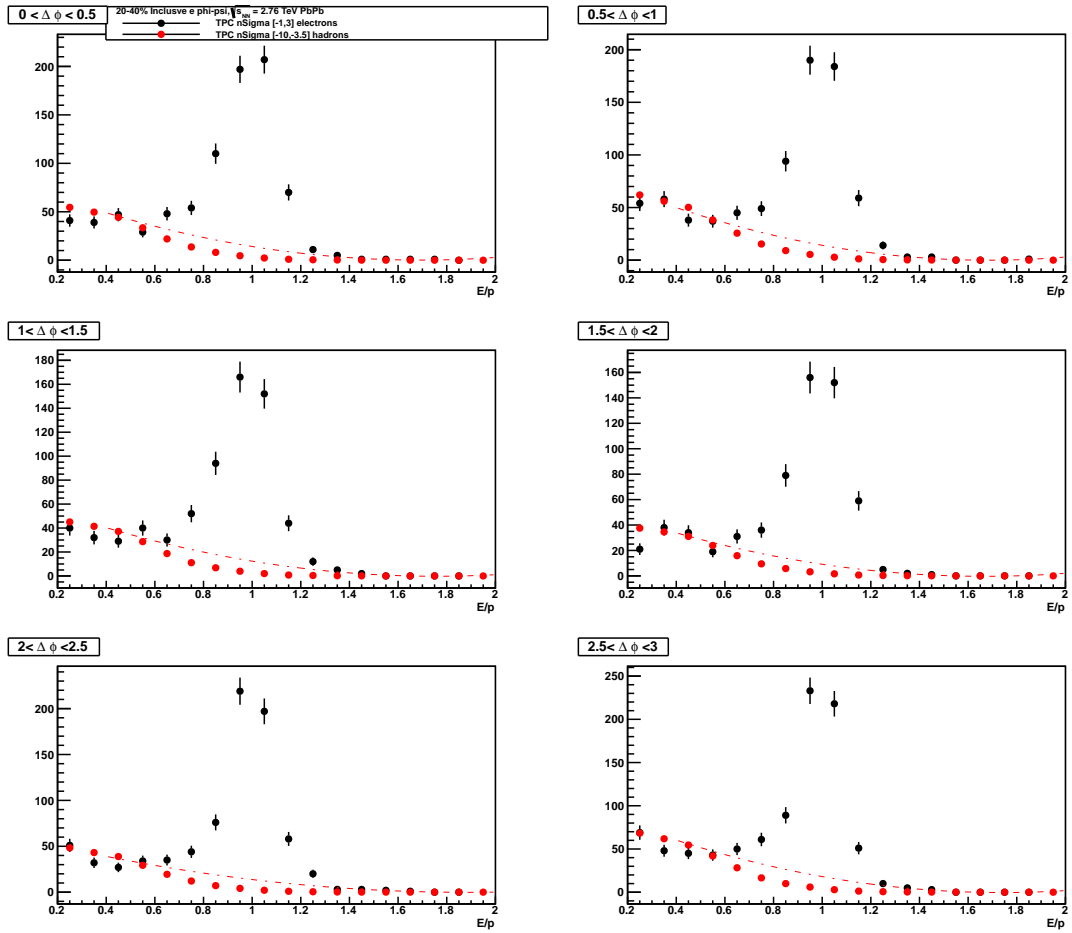


Figure 61:  $E/p$   $2 < p_T < 2.5$



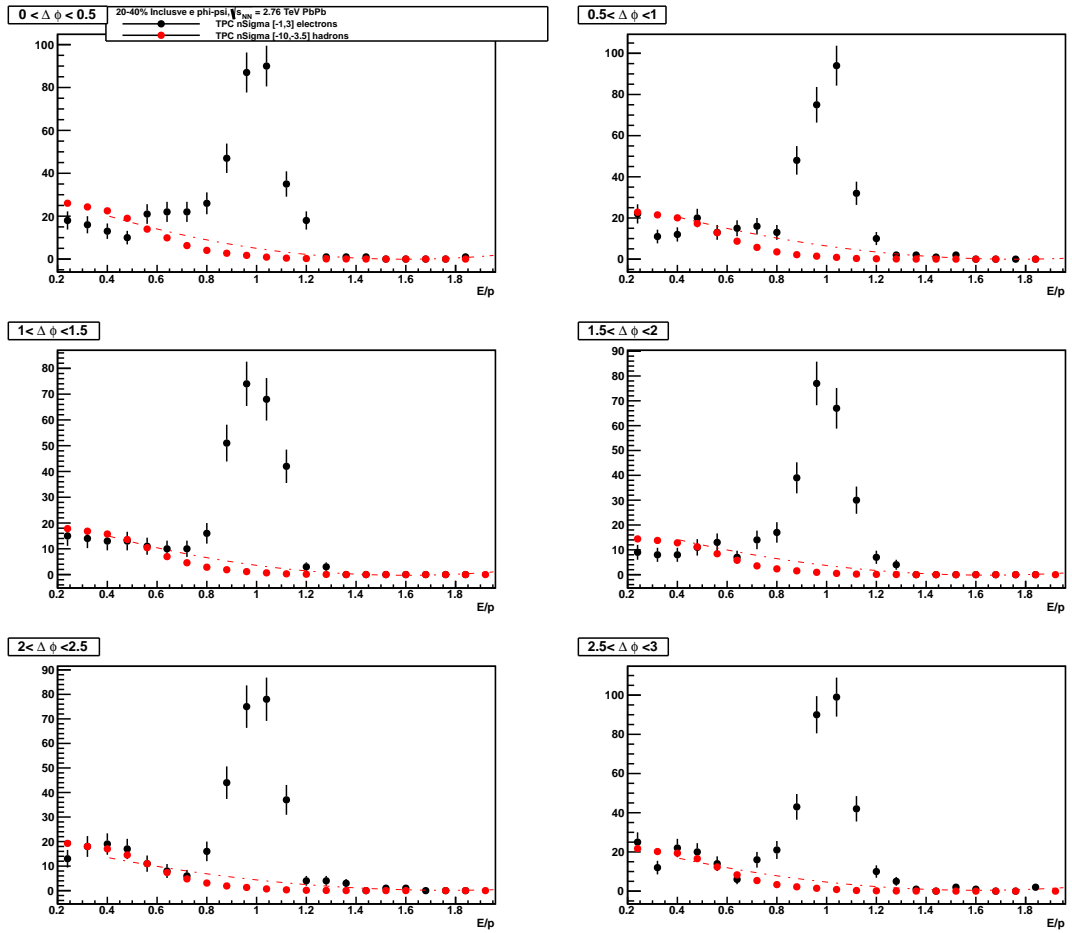


Figure 62:  $E/p$   $2.5 < p_T < 3$

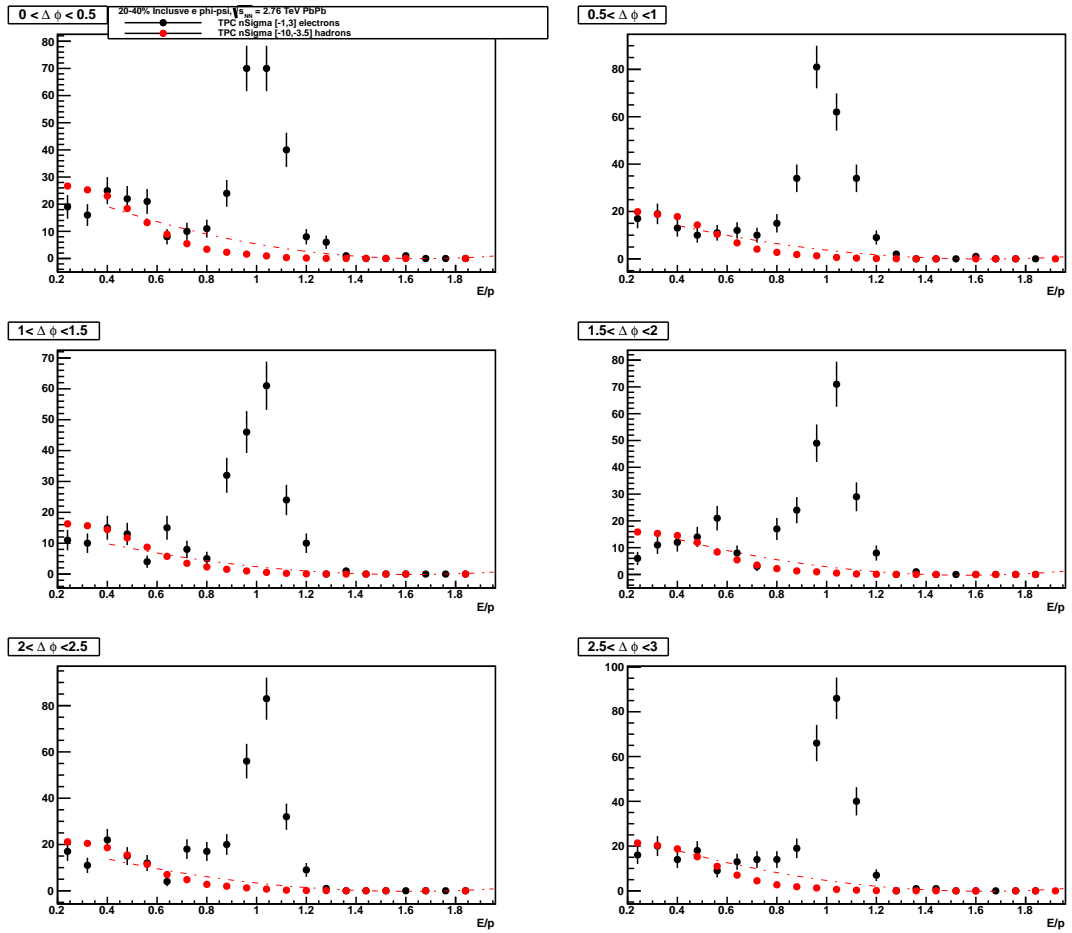


Figure 63:  $E/p$   $3 < p_T < 4$

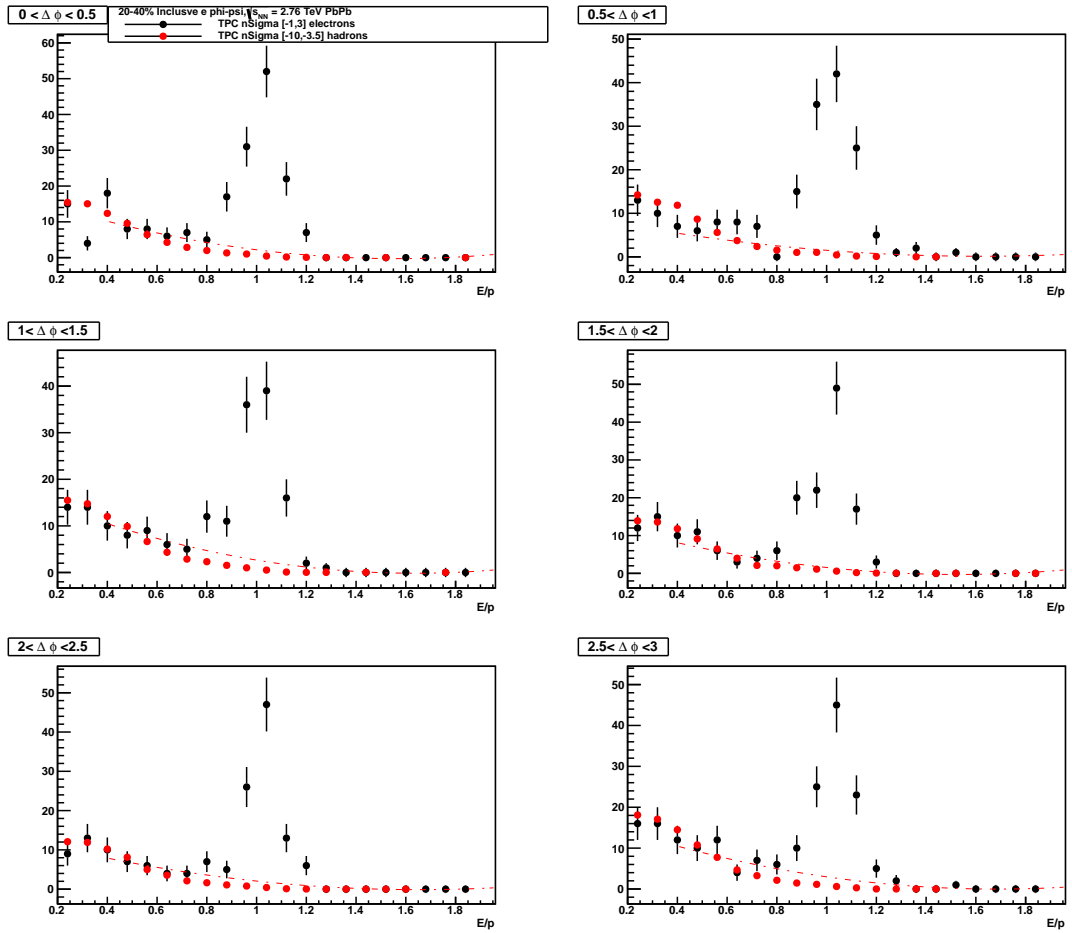


Figure 64:  $E/p$   $4 < p_T < 6$

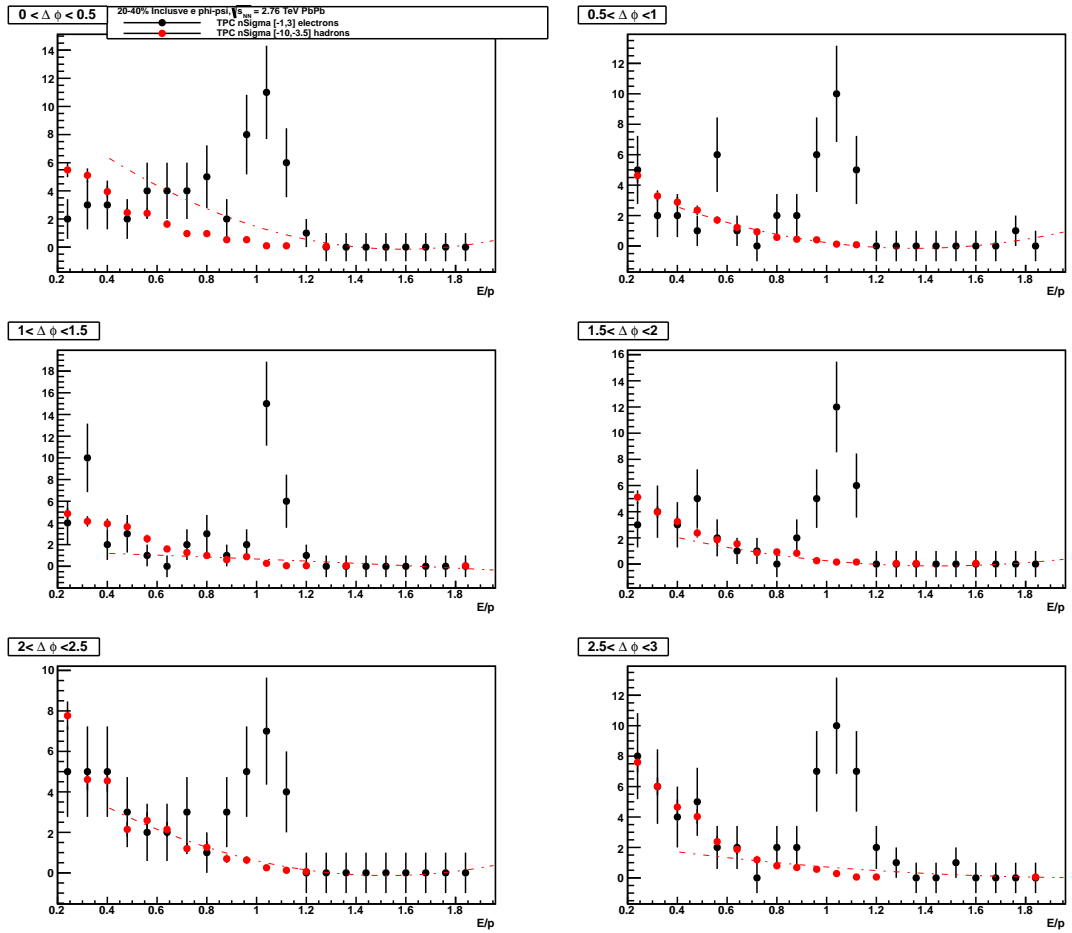


Figure 65:  $E/p$   $6 < p_T < 8$

## References

- [1] Aamodh, K.: *Elliptic Flow of Charged Particles in Pb-Pb Collisions at  $\sqrt{s_{NN}} = 2.76$  TeV* Physical Review Letters 17 December 2010
- [2] K. Aamodt, K. et al.: *The ALICE experiment at the CERN LHC* IOP-science 2008
- [3] Aitchison, I.J.R., Hey, A.J.G.: *Gauge Theories in Particle Physics: Volume I: From Relativistic Quantum Mechanics to QED* 2004, 3rd edition.
- [4] Bairathi, V.: *Study of Elliptic Flow of Identified Charge Particles using Relativistic Heavy-ion Collision Models using Different Flow Methods* Summer Training Project Report 2010-2011
- [5] Cowan, G.: *Statistical Data Analysis (Oxford Science Publications)* 1998
- [6] Halzen, F., Martin, A.D.: *Quarks & Leptons: An introductory course in modern particle physics* 1984
- [7] Hirano, T., Heinz, U.W., Kharzeev, D. et al.: *491) Hadronic dissipative effects on transverse dynamics at RHIC*. J. Phys., 2007
- [8] Huovinen, P., Petreczky, P.: *QCD Equation of State and Hadron Resonance Gas* Nucl. Phys., 2010
- [9] James, F.: *Statistical Methods in Experimental Physics* 2006
- [10] V. L. Korotkikh, I. P. Lokhtin, S. V. Petrushanko, L. I. Sarycheva, A. M. Snigirev, G. Kh. Eyyubova: *Elliptic flow of particles in heavy-ion collisions and possibility of its observation at the LHC energies* Physics of Atomic Nuclei Volume 71, Issue 12, 01 December 2008
- [11] Lin, Q.W., Ko, C.M.: *Elliptic Flow in Heavy Ion Collisions at RHIC*
- [12] Ollitrault, J.-Y.: *Anisotropy as a signature of transverse collective flow* Phys. Rev. D 46, 229, 1992
- [13] Snellings, R.: *Elliptic Flow: A Brief Review* 16 June 2011
- [14] Taylor, J.R.: *An introduction to Error Analysis* 1939
- [15] The ALICE collaboration